High-pressure phase stability and thermoelastic properties of iron carbonitrides and nitrogen in the deep Earth

Shengxuan Huang[1,2,3], Xiang Wu[3], Feng Zhu[2], Xiaojing Lai[4], Jie Li[5], Owen K. Neill[5], Shan Qin[1], Robert Rapp[2], Dongzhou Zhang[2,6], Przemyslaw Dera[2], Stella Chariton[6], Vitali B. Prakapenka[6], and Bin Chen[2]

[1]Key Laboratory of Orogenic Belts and Crustal Evolution, MOE, Peking University and School of Earth and Space Sciences, Peking University, Beijing, China

[2]Hawai'i Institute of Geophysics and Planetology, University of Hawai'i at Mānoa, Honolulu, HI, USA

[3]State key laboratory of geological processes and mineral resources, China University of Geosciences, Wuhan, China

[4]Gemmological Institute, China University of Geosciences, Wuhan, China

[5]Department of Earth and Environmental Sciences, University of Michigan, Ann Arbor, MI, USA

[6]Center for Advanced Radiation Sources, University of Chicago, Chicago, IL, USA

Corresponding author: Bin Chen: binchen@hawaii.edu; Xiang Wu: wuxiang@cug.edu.cn

Key Points:

- ε-type iron carbonitrides undergo two phase transitions at high pressure and high temperature.

- N/C and Fe/(N+C) atomic ratios are two key factors affecting the phase stability and elasticity of iron carbonitrides.

- Iron carbonitrides with diverse structures may be the main host for nitrogen in the deep mantle and encapsulated in superdeep diamonds.

Abstract

Iron-dominant metallic phases are likely the primary hosts for nitrogen in the reduced deep Earth, hence the storage of nitrogen in the lower mantle and the core is governed by the behavior of the Fe-N-C system at high temperatures and pressures. In this study, phase transitions and thermoelastic properties of iron carbonitrides were investigated at high pressure-temperature conditions by diamond anvil cell experiments and first-principles calculations. Experimental data revealed no phase transition in ε-type $Fe_4(N_{0.6}C_{0.4})$ or $Fe_7(N_{0.75}C_{0.25})_3$ up to 60 GPa at room temperature. At high temperature $Fe_7(N_{0.75}C_{0.25})_3$ transforms into the Fe_3C-type phase at ~27 GPa, and then into the Fe_7C_3-type phase at ~45 GPa, which is also corroborated by our theoretical calculations. We found that the phase stability of iron carbonitrides mainly depends on the N/C ratio, and the elastic properties of iron carbonitrides are dominantly affected by the Fe/(N+C) ratio. Iron carbonitrides with diverse structures may be the main host for nitrogen in the deep mantle. Some iron carbonitride inclusions in lower mantle diamonds could be the residue of the primordial mantle or originate from subducted nitrogen-bearing materials, rather than iron-enriched phases of the outer core. In addition, our experiments confirmed the existence of Fe_7C_3-type Fe_7C_3-Fe_7N_3 solid solutions above 40 GPa. Fe_7C_3-type $Fe_7(C,N)_3$ has comparable density and thermoelastic properties to its isostructural endmembers and may be a promising candidate constituent of the Earth's inner core.

Plain Language Summary

Nitrogen is an essential element for the Earth's atmosphere and life. Most of the Earth's nitrogen may reside in Earth's interior, which may profoundly influence the partial pressure of atmospheric nitrogen. Knowledge on the storage and cycling of nitrogen in the deep Earth is crucial for our understanding of the Earth's evolution and dynamics. We combined high-pressure and high-temperature experiments and theoretical calculations to investigate the phase transitions and elasticity of iron carbonitrides. The results show that iron carbonitrides are stable upon compression at room temperature, but transformed into two high-pressure structures at lower pressures at high temperatures than their iron carbide counterparts. N/C and Fe/(N+C) atomic ratios are two key factors affecting the phase stability and elasticity of iron carbonitrides. Nitrogen could be stored in the Earth's lower mantle in the form of iron carbonitrides. Iron carbonitrides may be the main nitrogen host and be trapped as inclusions in some superdeep diamonds and carried to the shallow regions through geodynamic processes, as we can find in some diamonds of sublithospheric origin.

1 Introduction

Nitrogen (N) is one of the most significant volatiles in our planet, an essential element for life, and the primary component of the atmosphere. Nitrogen in the Earth's interior is linked to that near the surface through processes of subduction and volcanic outgassing, influencing the partial pressure (*P*) of atmospheric N in a profound way (Busigny et al., 2019; Mikhail and Sverjensky, 2014). This "deep nitrogen" also provides crucial insights into planetary evolution, including the accretion and differentiation of the core and mantle on Earth, as well as the delivery of late veneers and the deep recycling of other volatiles associated with N (Bergin et al., 2015; Dalou et al., 2017; Grewal et al., 2019b; Kaminsky and Wirth, 2017). Based upon the abundance of N in the bulk

Earth relative to that measured in carbonaceous chondrites, the bulk Earth is depleted by an order of magnitude in N in comparison with other volatiles, which is the so-called "missing nitrogen" problem (Marty, 2012). A recent study by Johnson and Goldblatt (2015) has suggested that N contents in the "deep Earth" may be considerably underestimated, and that more than 90% of the bulk Earth N content is likely to be residing in these hidden and largely 'inaccessible' reservoirs. Core-mantle differentiation represents a first-order process controlling the initial distribution of N among the various reservoirs in the deep Earth. The partitioning behavior of N between iron-enriched alloys and silicates can be affected by P, temperature (T), and the composition of the participating phases, but the prevailing oxygen fugacity (f_{O_2}) appears to be the dominant factor (Dalou et al., 2017; Grewal et al., 2019a, b; Roskosz et al., 2013). At realistic P-T-f_{O_2} conditions for core formation (i.e. 40~60 GPa, 3000~4000 K and IW-3~0), N prefers to bond with iron (Fe), and is incorporated more into the Earth's core than into the silicate mantle. On the other hand, the silicate mantle may be saturated with Fe at depths >250 km, and Fe concentration can reach ~1 wt% in the lower mantle due to disportionation of Fe^{2+} and preferential incorporation of Fe^{3+} in bridgmanite (Frost et al., 2004). The partition coefficient for N between metallic Fe and bridgmanite is close to 100, indicating that the N content of the metallic phase in the lower mantle should be nearly equivalent to that of the rest of the silicate lower mantle (Yoshioka et al., 2018). Therefore, the Fe-enriched metallic phase is likely to be a main host for N in the Earth's interior. A more complete picture of the N evolution of the Earth requires the determination of the composition and stability of N-bearing Fe-enriched minerals at high P-T conditions.

In the Fe-N system, several Fe nitrides are stable at ambient conditions, including cubic γ'-Fe_4N (space group: $Pm\overline{3}m$), orthorhombic ζ-Fe_2N (space group: $Pbcn$) and nonstoichiometric ε-type Fe_3N_x (Wriedt et al., 1987). The space group of ε-type Fe_3N_x has been assigned to either $P3_12$ or $P6_322$, in which N atoms occupy part of the octahedral vacancies. The ε-type Fe_3N_x is capable of holding a range of N in its structure, with x varying from 0.6 to 1.5 (Fig. S1) (Litasov et al., 2017; Niewa et al., 2009a). At 9~15 GPa and 1400~1600 K, Fe_4N and Fe_2N undergo structural transitions to ε-type phases (Guo et al., 2013; Niewa et al., 2009b; Schwarz et al., 2009). The ε-type Fe_3N_x is stable up to ~40 GPa and ~1500 K (Litasov et al., 2017; Minobe et al., 2015). Upon further compression, ε-type Fe_3N_x transforms into Fe_7C_3-type Fe_7N_3 (Minobe et al., 2015). As compared to the ε-type phase, Fe_7C_3-type Fe_7N_3 is stable over a much broader P-T range, i.e., to at least ~150 GPa and ~3000 K (Kusakabe et al., 2019; Minobe et al., 2015). These results suggest that, among various Fe nitrides, ε-type Fe_3N_x and Fe_7C_3-type Fe_7N_3 are strong candidates for the storage hosts of N in the Earth's mantle and core.

Because of relatively low abundance of N in the bulk Earth, it is likely that, in addition to forming pure Fe nitrides, N substitutes for other light elements into the crystal structures of Fe-enriched alloys. Carbon (C) has similar geochemical and cosmochemical properties to N. They may mutually coexist and replace each other to form solid solutions in deep reservoirs (Sagatov et al., 2019). Indeed, recent studies have reported various Fe carbonitrides and nitrocarbides, such as $Fe_9(N_{0.8}C_{0.2})_4$, $Fe_5(C_{0.48}N_{0.52})_2$ and $Fe_7(C_{0.73}N_{0.27})_3$, inclusions in superdeep diamonds (Kaminsky and Wirth, 2017). A recent study shows that N could replace C in Fe_3C to form an ε-type C-bearing Fe_3N_x at 7~17 GPa, indicating that N appears to have a better affinity to Fe than C at high P-T conditions (Litasov et al., 2016). The combined effects of N and C in the Fe-enriched Fe-N-C system under simultaneous high-P and high-T conditions provide indispensable clues to decipher the storage and speciation of N in the Earth's mantle and core. Sokol et al. (2017) have recently reported a complex phase diagram for the Fe-enriched Fe-N-C system at 7.8 GPa and 1350 ºC.

However, there are no experimental or theoretical studies to examine the phase stability and physical properties of Fe-N-C compounds at high *P-T* conditions. In this paper, we report the phase transitions and thermoelastic properties of two synthetic Fe carbonitrides of different stoichiometry at extreme conditions up to 60 GPa and 2000 K, as determined in experiments carried out using externally-heated and laser-heated diamond anvil cells (EHDAC and LHDAC) combined with synchrotron-based X-ray diffraction (XRD). In addition, first-principles calculations based on density functional theory (DFT) were performed to complement our experimental observations. Our results not only contribute to an improved understanding of the speciations of N stored in the Earth's deep interior but also shed light on the formation mechanism of Fe-N-C inclusions in lower mantle diamonds.

2 Materials and Methods

2.1 Sample synthesis and characterization

Two ε-type Fe carbonitrides were synthesized at high *P-T* conditions using a 2000-ton multi-anvil press at the University of Hawai'i at Mānoa. Starting materials were the mixtures of Fe_3N powder and synthetic Fe_3C. The Fe_3N powder was commercially obtained from Kojundo Chemical Lab. Co. Ltd. The Fe_3C sample was synthesized from a mixture of Fe powder (99.9+% purity, Aldrich Chemical Company) and graphite powder (99.9995% purity, Alfa Aesar Company) at an atomic ratio of Fe:C = 3:1 at 3 GPa and 1300 K for 8 hours using a MgO capsule and a graphite heater. The first ε-type Fe carbonitride sample was synthesized at 8 GPa and 1500 K for 1.5 hours using a MgO capsule and a 14/8 cell assembly (Liu et al., 2020). The synthesis of the second ε-type Fe carbonitride sample was carried out at 9 GPa and 1400 K for 20 hours using a MgO capsule and a 10/5 cell assembly (Leinenweber et al., 2012).

Back-scattered electron (BSE) images of individual samples were collected using the scanning electron microscope (SEM) on Cameca SX100 at the Robert B. Mitchell Electron Microbeam Laboratory (RM-EML), Department of Earth and Environmental Sciences, University of Michigan, Ann Arbor, and School of Earth and Space Sciences, Peking University. BSE images show that each synthetic sample consists of a homogeneous phase, and in addition to Fe carbonitride product, there is little graphite in the first sample (Fig. S2).

Concentrations of Fe, N and C were determined by Cameca SX100 electron probe microanalysis (EPMA) at the RM-EML, using a procedure similar to that of von der Handt and Dalou (2016) and Dalou et al. (2017). The accelerating potential was 10 kV, the beam current was 200 nA and the beam spot was focused to 1 μm. Fe Kα X-rays were measured using a large LiF diffracting crystal, using synthetic Fe_3C as a calibration standard; N Kα X-rays were measured using a large PC0 pseudocrystal (W/Si multilayer, 2d ≈ 4.5 nm), using synthetic Si_3N_4 as a calibration standard; and C Kα X-rays were measured using a PC2 diffracting crystal (Ni/C multilayer, 2d ≈ 10 nm), using synthetic Fe_3C as a calibration standard. Wavelength scans were performed around the Fe Kα, N Kα, and C Kα peaks to accurately determine the off-peak spectrometer positions for measuring continuum, and for modeling the continuum curvature (von der Handt and Dalou, 2016). For N Kα measurements, widely-spaced off-peak positions were used when measuring the Si_3N_4 standard due to the broadness of the N Kα peak from Si_3N_4. Off-peak measurements were made significantly closer to the peak on Fe-N-C samples, in order to reduce the uncertainty of the interpolation and to avoid the interference of the nearby second Bragg order Fe Lα and Lβ lines with the off-peak measurements (Fig. S3); these intensities of these lines are

significantly reduced by the PC0 pseudocrystal, but they are not fully suppressed even when differential pulse-height analyzer mode is used. Continuum intensities at the on-peak positions were interpolated from off-peak continuum measurements using an exponential function for N Kα and C Kα and a linear function for Fe Kα (von der Handt and Dalou, 2016). Counting times for all measured X-ray lines were 20 seconds on the peak and 10 seconds on each off-peak position. Samples were coated with ~15 nm of aluminum prior to analysis. In order to minimize the effects of differential coating thicknesses, calibration standards and Fe-N-C samples used in this study were coated at the same time. A liquid nitrogen cold finger was used to minimize carbon contamination of the sample surface during analysis, and a small time-dependent intensity correction was applied to N Kα and C Kα count rate data to account for changes in X-ray intensity due to degradation of the sample or conductive coating during analysis; no systematic changes in Fe Kα count rates over the course of the analyses were observed. Concentrations were calculated from measured, continuum-corrected X-ray intensities using the PROZA matrix corrections and the FFAST mass absorption coefficients (von der Handt and Dalou, 2016). In addition, an interference correction was applied to the measured N Kα intensities, to account for intensities contributed from the second Bragg order Fe Lβ3 and Lβ4 lines near the N Kα peak (Fig. S3); the magnitude of the correction was <5%. Suitable secondary standards containing Fe, N and C were not available to verify accuracy. In lieu of such materials, a synthetic, nominally nitrogen-free Fe-C sample was measured to verify that N concentrations were at or near zero. The N concentration measured in this material was 10 ± 250 μg/g. Also, any measurements with analytical totals of less than 98.5% or greater than 101.5% were excluded.

EPMA results show that the two samples are chemically homogeneous, with the average composition of the first sample as $Fe_4(N_{0.6}C_{0.4})$, and the second sample as $Fe_7(N_{0.75}C_{0.25})_3$ (Table S1). The crystal structures of these two samples were determined by XRD at beamline 13-BMC, Advanced Photon Source (APS), Argonne National Laboratory (ANL). The XRD measurements confirm that both the $Fe_4(N_{0.6}C_{0.4})$ and $Fe_7(N_{0.75}C_{0.25})_3$ phases adopt the ε-type structure.

2.2 High P-T synchrotron XRD experiments

BX90-type DACs with diamond anvils of 250 μm (in run-1, 2 and 4) or 300 μm (in run-3) were used to generate high P in four experimental runs. 130~160 μm diameter holes were drilled in pre-indented 30~35 μm rhenium gaskets to serve as sample chambers. $Fe_4(N_{0.6}C_{0.4})$, with a thickness of ~15 μm, was loaded into the sample chamber for run-1, with $Fe_7(N_{0.75}C_{0.25})_3$ comprising runs 2 and 3. A piece of Au foil placed near the sample was used to determine the internal P in all three of these runs (Fei et al., 2007). Neon gas was loaded as the P-transmitting medium (PTM) and ruby spheres were also loaded into the sample chamber to measure the P for the gas loading. In run-3, three Pt-10 wt% Rh (0.01'') wires wound around a pyrophyllite ring base allowed us to heat the sample to a maximum T of 750 K, and two K-type thermocouples (Chromega-Alomega 0.005'' and Chromega-Alomega 0.01'') in contact with the "downstream" diamond were used to measure the T (Lai et al., 2020). The difference in measured temperatures between these two thermocouple junctions was smaller than 15 K. In run-4, $Fe_7(N_{0.75}C_{0.25})_3$ with a thickness of ~10 μm was sandwiched between two KCl plates. In this arrangement, KCl acts as a PTM, a thermal insulator, and as a P indicator (Tateno et al., 2019).

Synchrotron XRD experiments of runs 1-3 were conducted at beamline 13-BMC, APS, ANL. The incident X-ray beam with a wavelength of 0.434 Å was focused to an area approximately 15 μm in diameter measured at the full width at half maximum. Membrane P control

system was used to increase P inside the DAC automatically. For the EHDAC experiment (run-3), XRD spectra were collected at four different temperatures (300 K, 450 K, 600 K and 750 K) at each given P. The LHDAC experiment (run-4) was performed at beamline 13-IDD, APS, ANL. The incident X-ray beam ($\lambda = 0.3344$ Å) had a focal spot size of 3×4 μm^2. The sample was heated gradually from both sides at intervals of 100~200 K at a given P using a double-sided laser heating system with the flat-top heating spot size of ~10 μm in diameter. A fresh spot of the sample was used for laser heating in each heating cycle. The T was determined by fitting the thermal radiation data using the Planck radiation function under the gray body approximation. The P at high T was determined from the volume of KCl using the thermal equation of state (EoS) (Tateno et al., 2019). The effective T of KCl was estimated according to Campbell et al. (2009) using the following approximation:

$$T_{\mathrm{KCl}} = \frac{3 \times T_{\mathrm{meas}} + 300}{4} \pm \frac{T_{\mathrm{meas}} - 300}{2}$$

The powder XRD spectra were integrated and then processed using model-biased Le Bail fitting with GSAS + EXPGUI software. For the single-crystal XRD spectra, the d-spacings of the sample at various P-T conditions were extracted using the GSE_ADA software, and lattice parameters were refined by the least-squares method. The P-volume (V) data were fitted using EoSFit7c software (Angel et al., 2014).

2.3 DFT-based first-principles calculations

DFT-based first-principles calculations were performed using the "projected augmented wave (PAW) method" as implemented in Vienna *ab-initio* simulation package (Kresse and Joubert, 1999). The exchange correlation potential was treated by the generalized gradient approximation (GGA) in the Perdew-Burke-Ernzerhof (PBE) version (Perdew et al., 1996). We chose the kinetic energy cut-off as 1000 eV in static simulations. The energy convergence criterion was 10^{-6} eV for electronic self-consistent calculations. The k-points grids were set as $7 \times 7 \times 7$, $6 \times 6 \times 8$ and $5 \times 5 \times 7$ in the Brillouin zone for the trigonal ε-type, orthorhombic Fe_3C-type and hexagonal Fe_7C_3-type structures, respectively. A $1 \times 1 \times 7$ supercell was constructed to simulate ε-type Fe_7N_3 and $Fe_7(N_{5/6}C_{1/6})_3$ phases. And a $1 \times 1 \times 2$ supercell was for ε-type $Fe_3(N_{0.75}C_{0.25})$ and h-type $Fe_7(N_{0.75}C_{0.25})_3$ phases. The total energy difference was converged to 10^{-5} eV/formula unit (f.u.) with respect to the energy cut-off or k-points. The corresponding force difference was converged to 10^{-3} eV/Å (less than 0.1 GPa). The spin-polarization of Fe without spin-orbit coupling was considered in the simulations. The ferromagnetic (FM) or nonmagnetic (NM) states were calculated for selected candidates. For each candidate phase, the cell parameters, atomic coordinates, and sublattice magnetic moments were allowed to relax at each given V. The calculated V-energy (E) data were fitted by the Birch-Murnaghan EoS to obtain the P-enthalpy (H) relation for each phase (Birch, 1947; Murnaghan, 1944):

$$E(V) = E_0 + \frac{9V_0K_0}{16}\left\{\left[\left(\frac{V_0}{V}\right)^{\frac{2}{3}} - 1\right]^3 K_0' + \left[\left(\frac{V_0}{V}\right)^{\frac{2}{3}} - 1\right]^2 \left[6 - 4\left(\frac{V_0}{V}\right)^{\frac{2}{3}}\right]\right\}$$

where E_0, V_0 and K_0 are the energy, unit-cell volume and isothermal bulk modulus at zero P, respectively. K_0' is the first P derivative of K_0. The derived H of each phase was compared with all the others to ascertain which phase is the most energetically favored at a given P and 0 K.

3 Results

3.1 Stability and phase transitions of iron carbonitrides

Four runs of experiments were conducted to investigate the stability of Fe carbonitrides at high P-T conditions up to ~60 GPa and ~2000 K (Fig. 1 and Table S2). No phase transition was observed at ambient T up to ~60 GPa in ε-type $Fe_4(N_{0.6}C_{0.4})$ (run-1) or to ~50 GPa in ε-type $Fe_7(N_{0.75}C_{0.25})_3$ (run-2) (Fig. S4). This indicates that the initial ε-type structure is stable over the studied P range at ambient T.
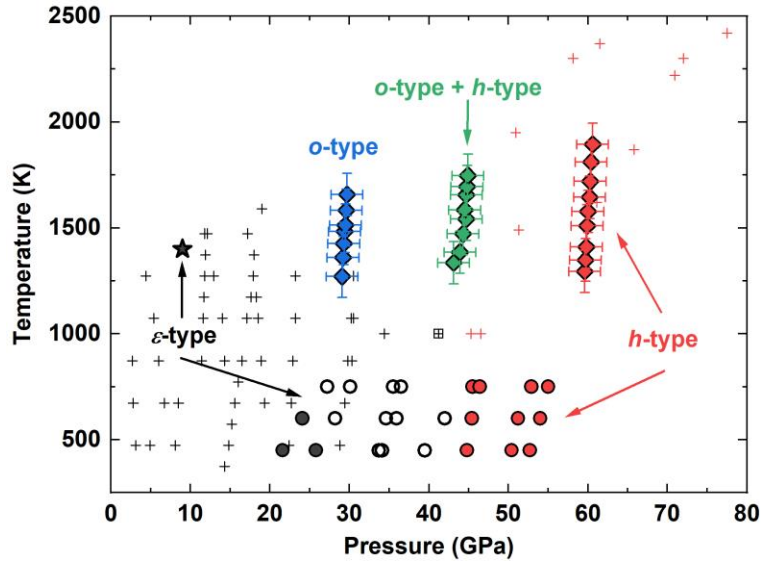
**Figure 1** Phase diagram of $Fe_7(N_{0.75}C_{0.25})_3$ at high P-T conditions. The ε-type, o-type and h-type represent the $P3_12$, Fe_3C-type ($Pnma$) and Fe_7C_3-type ($P6_3mc$) phases, respectively. The black star represents the synthetic conditions of ε-type $Fe_7(N_{0.75}C_{0.25})_3$ (9 GPa and 1400 K). The open circles represent the metastable ε-type phase at 27~40 GPa and 450~750 K. The open grey and red crosses represent the ε-type and h-type phases in the Fe-N binary system, respectively (Litasov et al., 2017; Minobe et al., 2015).
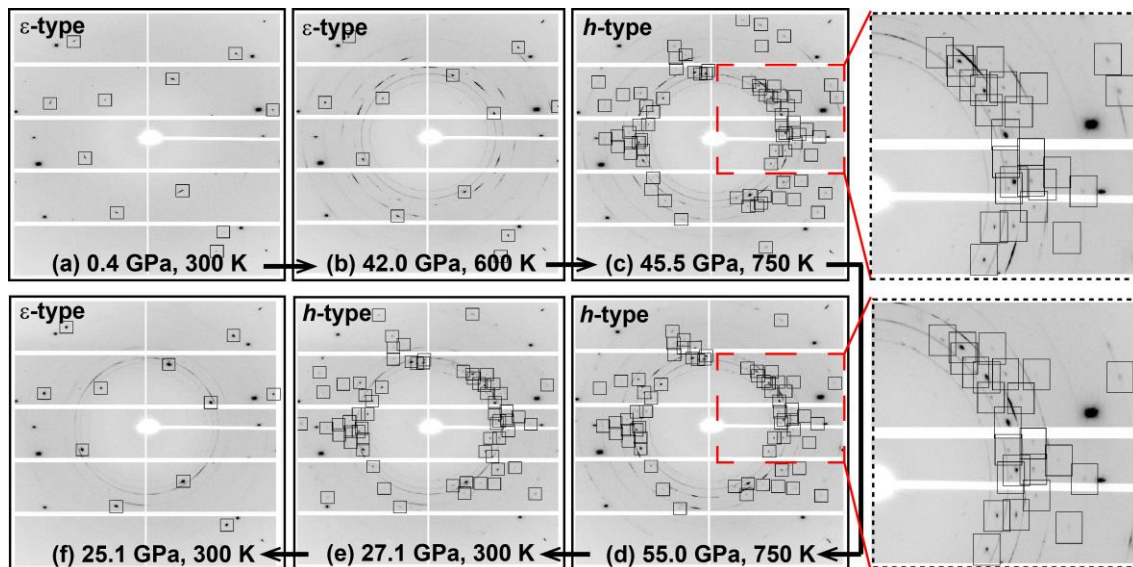
Figure 2 Representative measured 2D XRD patterns of $Fe_7(N_{0.75}C_{0.25})_3$ at high *P-T* conditions in run-3. The ε-type and *h*-type represent the $P3_12$ and Fe_7C_3-type ($P6_3mc$) structures, respectively.

      In run-3, ε-type $Fe_7(N_{0.75}C_{0.25})_3$ was observed to be stable to 42.0 GPa and 600 K (Fig. 2b); at 45.5 GPa and 750 K, the diffraction spots belonging to the ε-type structure disappeared and a few new spots appeared, implying the occurrence of a phase transition (Fig. 2c). This new phase is stable up to 55.0 GPa and 750 K (Fig. 2d), the highest *P-T* conditions achieved in run-3. When this phase was decompressed to 25.1 GPa at 300 K, it transformed back into the initial ε-type phase (Fig. 2f), demonstrating that the detected phase transformation was reversible. The observed new spots could be indexed by a hexagonal structure with lattice parameters $a = 6.584(1)$ Å, $c = 4.278(2)$ Å and $V = 160.62(9)$ Å^3 at 44.1 GPa and 300 K (Table S3). These values are very similar to those of hexagonal Fe_7C_3 and Fe_7N_3 (space group: $P6_3mc$, denoted as *h*-type) at equivalent *P* (Chen et al., 2012; Minobe et al., 2015). Therefore, an *h*-type structure was selected to solve the integrated 1-D XRD pattern, and the refinement results suggest that the new high-*P* phase can indeed be assigned to the *h*-type structure (Fig. S5).
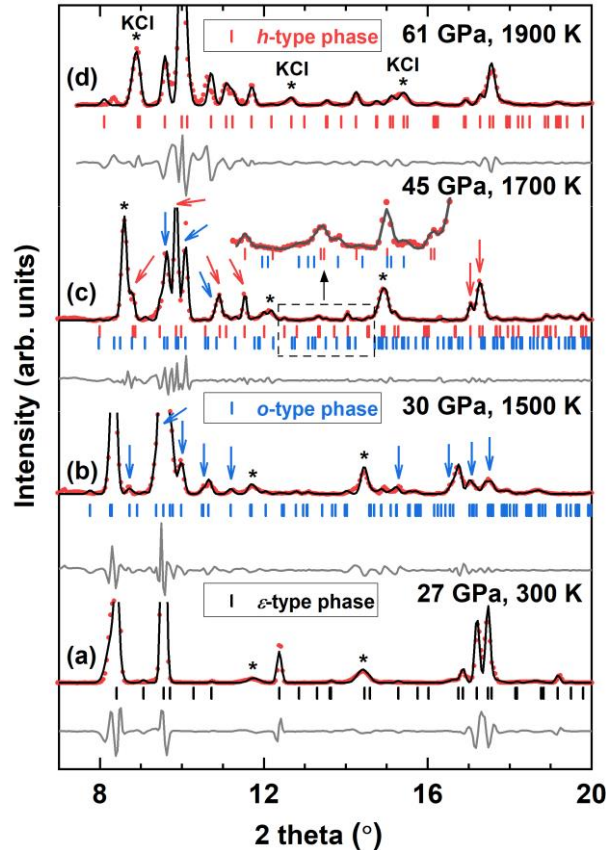
Figure 3 Representative measured XRD patterns of $Fe_7(N_{0.75}C_{0.25})_3$ at high *P-T* conditions in run-4. Le Bail refinements (black solid curves) of observed XRD data (red dots) were carried out after background subtraction. The difference curves (grey continuous line) between observed and calculated spectra are shown. The stars represent Bragg peaks of KCl. The black, blue, and red ticks represent Brag peaks of ε-type ($P3_12$), *o*-type (Fe_3C-type, *Pnma*), and *h*-type (Fe_7C_3-type, $P6_3mc$) phases, respectively.

In run-4, ε-type $Fe_7(N_{0.75}C_{0.25})_3$ was compressed to ~27 GPa at 300 K and then laser-heated, and we observed the Bragg peak intensities of the ε-type phase gradually decreased whereas a few new peaks emerged (Fig. 3b). The new phase can be assigned to a Fe_3C-type structure (space group: *Pnma*, denoted as o-type). The refined lattice parameters of the quenched o-type phase were determined to be $a = 4.892(2)$ Å, $b = 6.525(2)$ Å, $c = 4.366(1)$ Å and $V = 139.38(4)$ Å^3 at 28 GPa and 300 K (Fig. S6b), values that are slightly higher than those of pure Fe_3C at the similar P (Prescher et al., 2012). The XRD pattern after quenching was similar to that during heating, and no Bragg peaks of the ε-type structure were observed (Fig. S7). When laser-annealed at ~40 GPa, the o-type and h-type phases coexisted, and the h-type phase was dominant under these conditions (Fig. 3c and S6c). After being laser-annealed at higher P, ~60 GPa, the initial ε-type $Fe_7(N_{0.75}C_{0.25})_3$ transformed directly into the h-type phase without undergoing an intermediate o-type phase (Fig. 3d and S6d).

DFT-based first-principles calculations were performed to investigate the phase transitions that were observed in run-3 and run-4 (Table S4). We first looked into the magnetic properties of the ε-type, o-type and h-type structures for the Fe-N, Fe-C and Fe-N-C systems. For the ε-type structure, the magnetic moments of Fe are slightly affected by the substitution of C for N, whereas they are anti-correlated with the Fe/(N+C) ratio (Fig. S8a), in agreement with previous calculations concerning the Fe-N system (Popov et al., 2015). The magnetic moments of Fe of all calculated ε-type phases decrease smoothly with P, indicating there occurs no spin transition occurs up to 50 GPa. For the o-type structure, Fe_3N, Fe_3C and $Fe_3(N_{0.75}C_{0.25})$ have similar average magnetic moments, and the substitution of C for N tends to slightly increase the difference between the magnetic moments of FeI and FeII (Fig. S8b-c). In particular, the magnetic moments of Fe in Fe_3C collapse to zero above ~55 GPa, indicating a FM-NM transition of Fe_3C. This is consistent with previous X-ray emission spectroscopy (XES) results (Chen et al., 2018). By contrast, such transition is not observed in the N-rich o-type phases. For the h-type structure, Fe_7N_3 and Fe_7C_3 have distinct sub-lattice magnetic properties, though they adopt the same crystal structure and have comparable average magnetic moments (Fig. S8d-e). Specifically, FeI has the largest magnetic moments in Fe_7N_3, whereas FeII does in Fe_7C_3. The average and sub-lattice magnetic moments of Fe decrease gradually with P for Fe_7N_3 and Fe_7C_3, and no spin transition is predicted to occur in the calculated P range. It should be noted that there is a discontinuity in the evolution of magnetic moments of Fe in Fe_7C_3 at 40~45 GPa. This phenomenon has not been observed by previous experiments such as Mössbauer spectroscopy (MS) or XES (Chen et al., 2012, 2014). But previous simulations have reported similar results (Litasov et al., 2015). The reason of the difference between experimental and theoretical results remains to be investigated.

The o-type Fe_3C phase appears to be the most stable over the P range of the calculations (0~65 GPa) (Fig. S9), in agreement with previous experimental results (Liu et al., 2016b). The difference in unit-cell volumes between experimental and calculated results for pure Fe_3C is less than 2%. The ε-type Fe_3N is predicted to undergo phase transitions to the o-type phase at 38 GPa and 0 K, then to an assemblage of h-type Fe_7N_3 and Fe at 55 GPa and 0 K (Fig. 4a). We only calculated the ε-type and h-type phases in a Fe_7N_3 stoichiometry, since simulations of o-type Fe_7N_3 were unfortunately beyond our computational capability. The ε-to-h transition of Fe_7N_3 is predicted to occur at ~57 GPa (Fig. 4b). We further considered the P-induced phase transition in the Fe-N-C ternary system with a fixed composition of $Fe_3(N_{0.75}C_{0.25})$. At 0 K, the ε-type $Fe_3(N_{0.75}C_{0.25})$ transforms into the o-type phase at 26 GPa, and further into an assemblage of h-

type $Fe_7(N_{0.75}C_{0.25})_3$ and Fe at 47 GPa (Fig. 4c). The calculated lattice parameters of o-type phases are as follows: a = 4.729 Å, b = 6.715 Å, c = 4.323 Å and V = 137.3 Å^3 for Fe_3N at 29 GPa, and a = 4.760 Å, b = 6.677 Å, c = 4.322 Å and V = 137.4 Å^3 for $Fe_3(N_{0.75}C_{0.25})$ at 28 GPa, respectively. The calculated unit-cell V of o-type Fe_3N is 1.8%~2.0% larger than that of isostructural Fe_3C (Fig. S10a), whereas the unit-cell V of o-type $Fe_3(N_{0.75}C_{0.25})$ lies in between those of Fe_3C and Fe_3N. These results imply that the substitution of N for C can enlarge the unit-cell V of o-type Fe_3C. Furthermore, this substitution tends to reduce the a axis, increase the b axis and slightly affect the c axis (Fig. S11b). It will correspondingly reduce the a/c ratio and increase the b/c ratio (Fig. S12b). The unit-cell V of the o-type phase detected at 28 GPa and 300 K is ~1.4% larger than that of pure Fe_3C as measured by single-crystal XRD experiments (Fig. S10a) (Prescher et al., 2012). The a/c ratio of the o-type phase in our experiments deviates from those of pure Fe_3C. Therefore, it is reasonable to propose that the o-type phase detected in run-4 is a N-enriched phase.
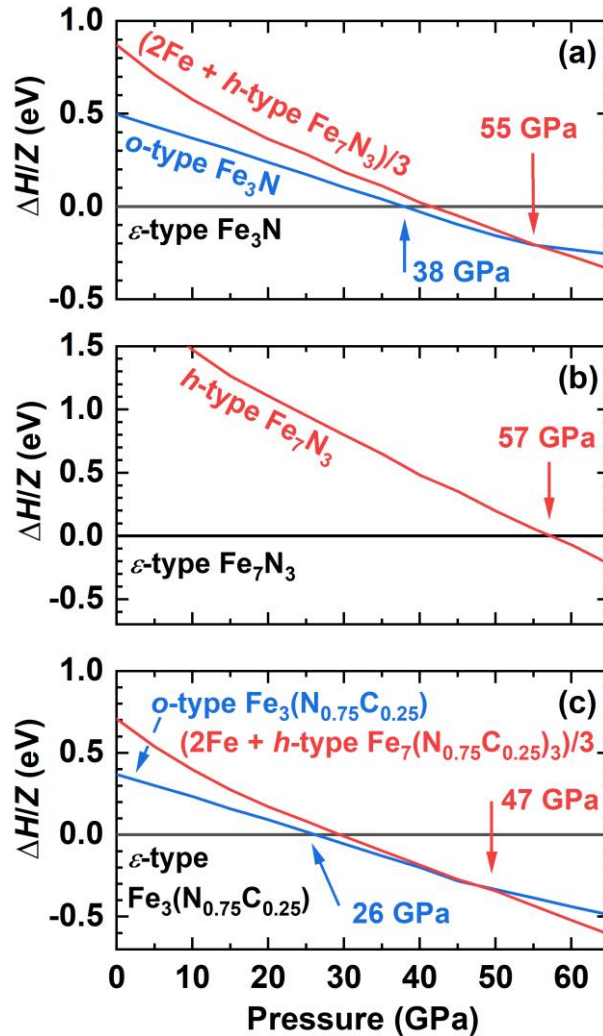

Figure 4 The calculated pressure-enthalpy relations of (a) Fe_3N, (b) Fe_7N_3 and (c) $Fe_3(N_{0.75}C_{0.25})$ with different structures. The ε-type, o-type and h-type represent the $P3_12$, Fe_3C-type ($Pnma$) and Fe_7C_3-type ($P6_3mc$) structures, respectively.

3.2 Thermoelastic properties of iron carbonitrides

The lattice parameters of the two ε-type samples in run-1 and run-2 were determined only to a P up to ~33 GPa: above this P, many of the Debye-Scherrer rings or spots associated with the Fe carbonitrides overlap with those associated with Re, the PTM, and Au (Table S5 and S6). The unit-cell volumes of the ε-type phases decrease monotonically with P, and no discontinuities in their P-V curves are observed (Fig. 5a). The room-T P-V data were fitted to the third-order Birch-Murnaghan EoS (Birch, 1947; Murnaghan, 1944):

$$P(V) = \frac{3}{2}K_0\left[\left(\frac{V_0}{V}\right)^{\frac{7}{3}} - \left(\frac{V_0}{V}\right)^{\frac{5}{3}}\right] \times \left\{1 + \frac{3}{4}(K_0' - 4)\left[\left(\frac{V_0}{V}\right)^{\frac{2}{3}} - 1\right]\right\}$$

The normalized stress (F_E) versus Eulerian strain (f_E) plot suggests that it is reasonable to fit the P-V data using one single equation of state over their respective pressure range (Fig. S13). In addition, the slope of the f_E-F_E curve for each ε-type sample is close to zero. The corresponding K_0' derived from the f_E-F_E relation is 3.94±0.25 for Fe$_4$(N$_{0.6}$C$_{0.4}$) and 4.15±0.12 for Fe$_7$(N$_{0.75}$C$_{0.25}$)$_3$. These results indicate that it is reasonable to fix K_0' as 4, and the V compressibility of ε-type Fe carbonitrides could be adequately described by the second-order Birch-Murnaghan EoS. The fitted parameters yield, for ε-type Fe$_4$(N$_{0.6}$C$_{0.4}$), $V_0 = 81.11(7)$ Å^3, $K_0 = 133(2)$ GPa, and $K_0' = 4$ (fixed). For ε-type Fe$_7$(N$_{0.75}$C$_{0.25}$)$_3$, the values are $V_0 = 85.00(1)$ Å^3, $K_0 = 177(1)$ GPa and $K_0' = 4$ (fixed) (Table S7). Fe$_7$(N$_{0.75}$C$_{0.25}$)$_3$ has a similar compressibility to pure Fe nitride and is less compressible than Fe$_4$(N$_{0.6}$C$_{0.4}$) (Fig. 5b and Table S7) (Adler and Williams, 2005; Litasov et al., 2014, 2017; Lv et al., 2020; Yin et al., 2014).
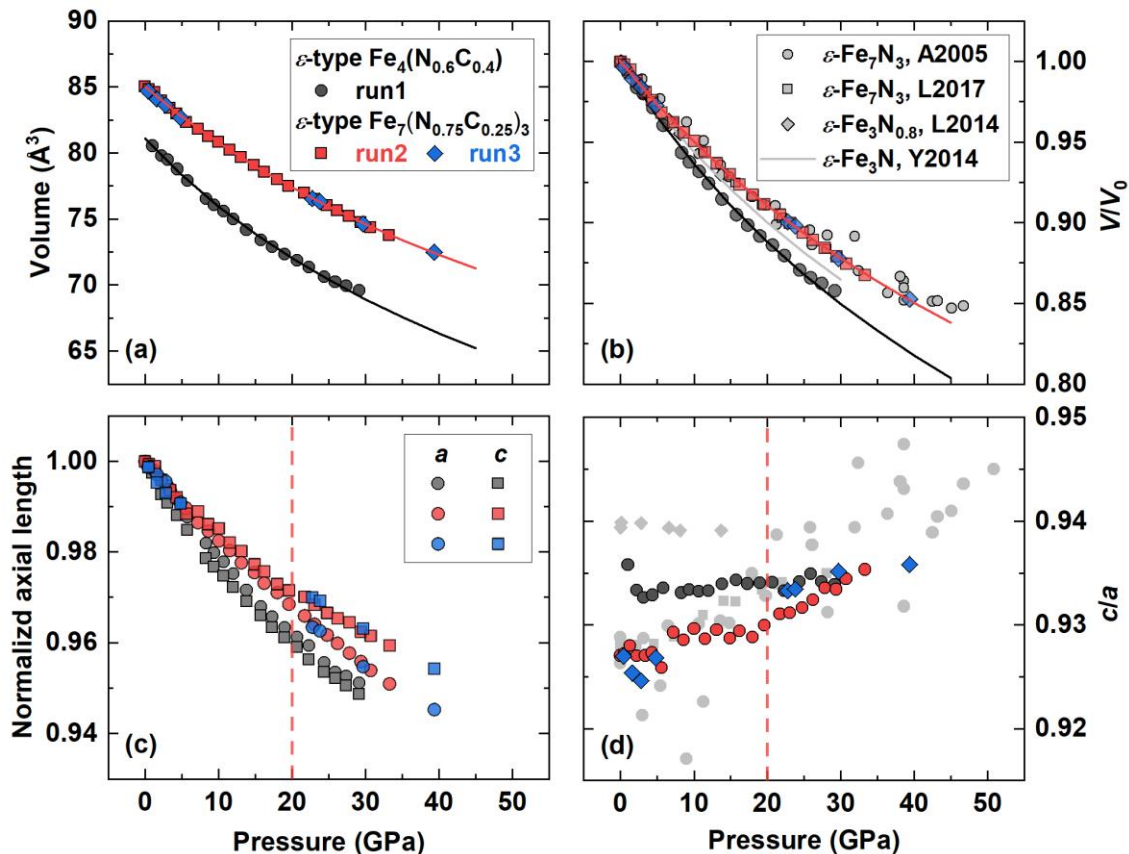
Figure 5 Evolution of (a) unit-cell V, (b) normalized V, (c) normalized axial length and (d) c/a ratio of ε-type $Fe_4(N_{0.6}C_{0.4})$ and $Fe_7(N_{0.75}C_{0.25})_3$ as a function of P at room T. The black and red solid curves are calculated using the Birch-Murnaghan equation of state parameters of ε-type $Fe_4(N_{0.6}C_{0.4})$ and $Fe_7(N_{0.75}C_{0.25})_3$, respectively. The red dashed line indicates the abnormal change in the relative axial compression and c/a ratio of ε-type $Fe_7(N_{0.75}C_{0.25})_3$. The uncertainties are within the symbols. Previous experimental data of ε-type Fe nitrides are plotted for comparison (Adler and Williams, 2005; Litasov et al., 2014, 2017; Yin et al., 2014).

The relative compression of crystal axes and the c/a ratio of the ε-type Fe carbonitrides at room T are shown in Fig. 5c-d. $Fe_4(N_{0.6}C_{0.4})$ is nearly isotropic in the axial direction and its c/a ratio is almost constant up to at least 30 GPa. The compressibility along the a axis of $Fe_7(N_{0.75}C_{0.25})_3$ is comparable to that along the c axis below 20 GPa, but becomes higher than the c axis above 20 GPa. This effect is also manifested in a change in the c/a ratio. The c/a ratio of $Fe_7(N_{0.75}C_{0.25})_3$ is systematically smaller than that of $Fe_4(N_{0.6}C_{0.4})$. Theoretical calculations show that the incorporation of N or C has a negligible effect on the c axis but increases the a axis (Fig. S11a). And the slope of the c/a ratio versus P of $Fe_7(N,C)_3$ is larger than that of $Fe_3(N,C)$ (Fig. S12a). Recent neutron diffraction experiments have found the magnetic moments of Fe oriented perpendicular to the c axis of the ε-type structure (Lei et al., 2018). The addition of more N or C into the ε-type structure enlarges the a axis and reduces the interactions of magnetic moments between Fe atoms, which results in a reduction of magnetic moments (Fig. S8). This will cause the a axis to become more compressible. The change of the c/a ratio of ε-type $Fe_7(N,C)_3$ is not observed in the present simulation. This change cannot result from the spin transition of Fe based on our calculations. It might be related to a change in the magnetic ordering of $Fe_7(N_{0.75}C_{0.25})_3$. However, since our first-principles calculations are performed at 0 K, the paramagnetic state cannot be simulated. Further MS experiments could provide direct evidence on the evolution of magnetic ordering of ε-type Fe carbonitride samples upon compression. Note that even if there is an anomaly in the relative compressibility of the axes, it exerts a negligible effect on the compressive properties of unit-cell V of ε-type $Fe_7(N_{0.75}C_{0.25})_3$ (Fig. S13).
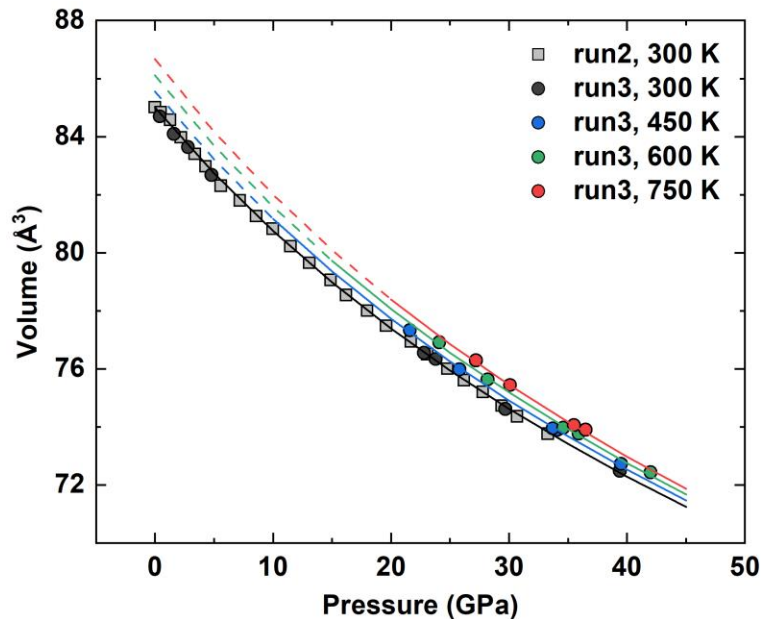
Figure 6 The P-V-T data of ε-type $Fe_7(N_{0.75}C_{0.25})_3$ fitted by the high-T Birch-Murnaghan equation of state. The solid and dashed curves are calculated using the Birch-Murnaghan equation of state parameters of ε-type $Fe_7(N_{0.75}C_{0.25})_3$. The P and V uncertainties are within the symbols.

The thermal EoS of our sample was derived from its room-T EoS and P-V data obtained at 450 K, 600 K and 750 K (Fig. 6). Assuming that the T dependence of isothermal bulk modulus at high temperature $\partial K/\partial T$ and the first P derivative of isothermal bulk modulus K_{T0}' are constant over the investigated P-T range, K_{T0} and K_{T0}' can be expressed as following:

$$K_{T0} = K_0 + \partial K/\partial T \times (T - 300)$$

$$K_{T0}' = K_0'$$

The T dependence of V at ambient P, V_{T0}, can be expressed as a function of thermal expansion coefficient α_T:

$$V_{T0} = V_0 exp\left(\int_{300}^{T} \alpha_T dT\right)$$

and due to limited V data at simultaneous high P-T conditions, the thermal expansion coefficient α_T is assumed to be constant by the approximation that $\alpha_T = \alpha_0$ (Berman, 1988). The fitted thermoelastic parameters for ε-type $Fe_7(N_{0.75}C_{0.25})_3$ are consequently $\partial K/\partial T = -0.02(1)$ GPa/K and $\alpha_0 = 3.3(8) \times 10^{-5}$ K^{-1} (Table S7).
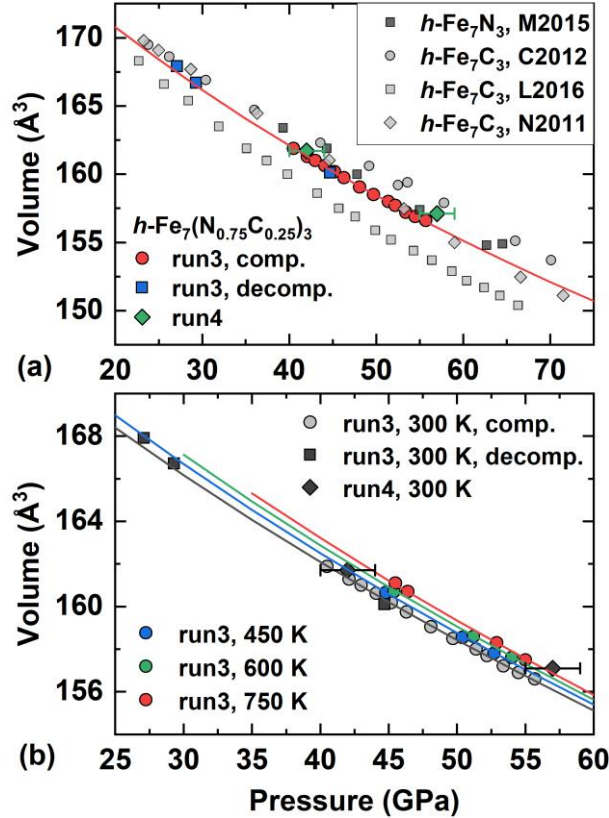
Figure 7 The P-V (a) and P-V-T (b) data of h-type $Fe_7(N_{0.75}C_{0.25})_3$. The solid curves are calculated using the Birch-Murnaghan equation of state parameters of h-type $Fe_7(N_{0.75}C_{0.25})_3$. The error bars

represent *P* uncertainties in run-4. The *P* and *V* uncertainties in run-3 are within the symbols. Previous experimental data of *h*-type Fe_7C_3 and Fe_7N_3 are plotted for comparison (Chen et al., 2012; Liu et al., 2016a; Minobe et al., 2015; Nakajima et al., 2011).

The refined lattice parameters and unit-cell volumes of *h*-type $Fe_7(N_{0.75}C_{0.25})_3$ at various *P-T* conditions are listed in Table S8. The unit-cell volumes of *h*-type $Fe_7(N_{0.75}C_{0.25})_3$ obtained in run-4 are generally consistent with the results of run-3 (Fig. 7a). However, because of the relatively large uncertainty in determining the *P* in run-4 using KCl, the room-*T* EoS of *h*-type $Fe_7(N_{0.75}C_{0.25})_3$ is calculated only using the *P-V* data during compression in run-3. The fitted parameters for *h*-type $Fe_7(N_{0.75}C_{0.25})_3$ are $V_0 = 182.4(7)$ Å^3, $K_0 = 268(9)$ GPa and $K_0' = 4$ (fixed). The compressibility of *h*-type $Fe_7(N_{0.75}C_{0.25})_3$ is generally comparable to that of the isostructural endmembers Fe_7N_3 and Fe_7C_3 (Fig. 7a and Table S9) (Chen et al., 2012; Kusakabe et al., 2019; Liu et al., 2016a; Minobe et al., 2015; Nakajima et al., 2011). The lattice parameters of $Fe_7(N_{0.75}C_{0.25})_3$ decrease smoothly with increasing *P* (Fig. S11c and S14). The *a/c* ratio of *h*-type $Fe_7(N_{0.75}C_{0.25})_3$ increases slightly with *P* as compared with Fe_7C_3, implying a weak anisotropy in the axial compressibility (Fig. S12c). Although there are some differences between experimental and theoretical data in terms of the absolute values, the calculated results generally follow the trend of the experimental ones. First-principles simulations have shown that N-rich $Fe_7(N,C)_3$ has distinct sub-lattice magnetic properties from Fe_7C_3. The Fe-Fe distance in the *ab* plane is shorter than that along the *c* axis in the *h*-type structure. FeII has the largest magnetic moments in Fe_7C_3 but it is the smallest in Fe_7N_3. Therefore, there exist stronger magnetic and electronic interactions between Fe atoms in the *ab* plane in Fe_7C_3 in comparison with Fe_7N_3. This contributes to different axial compression behaviors of *h*-type Fe_7C_3 and N-rich $Fe_7(N,C)_3$. We also calculated the thermal EoS of *h*-type $Fe_7(N_{0.75}C_{0.25})_3$ with the following fitted results: $\partial K/\partial T = -0.046(34)$ GPa/K and $\alpha_0 = 3.2(1.5) \times 10^{-5}$ K^{-1} (Fig. 7b).

4 Discussion

Previous experiments have reported that *ε*-type Fe_7N_3 transforms directly into the *h*-type structure above 40 GPa at high *T*, and the *o*-type phase has not been observed between 20 and 40 GPa (Minobe et al., 2015). Our static calculations have shown that *o*-type Fe_3N becomes energetically favorable in comparison with *ε*-type Fe_3N above 38 GPa. But the *ε*-to-*o* transition is only evaluated in the Fe_3X stoichiometry due to our limited computational capability. The *o*-type Fe_3C is found to have a wide solid solution range depending on the synthetic conditions. The *o*-type Fe_3C with C-deficiency up to 2.6 at% ($Fe_3C_{0.87}$) is synthesized at Fe-saturated conditions, and that containing 28 at% C ($Fe_3C_{1.17}$) is detected at C-saturated conditions (Walker et al., 2013, 2015; Zhu et al., 2019b). Adding much more C to stoichiometric Fe_3C tends to destabilize the *o*-type phase and finally leads to forming *h*-type Fe_7C_3. If this can be applied in the Fe-N system, the present calculations may overestimate the stability of the *o*-type Fe nitride. The incorporation of C in the Fe-N system can lower the two transition pressures and slightly expand the stability field of the *o*-type phase, which may facilitate the observation of this phase in Fe carbonitrides. However, given the structural characteristics of the *o*-type phase, the *ε*-to-*o* transformation of $Fe_7(N_{0.75}C_{0.25})_3$ will be accompanied by a partial dissociation, causing its composition to approach the Fe_3X stoichiometry. Recent studies have found that deviation from the stoichiometric composition of Fe_3C in either C-deficiency or C-excess direction reduces the unit-cell *V* (Walker et al., 2013, 2015; Zhu et al., 2019b). This finding indicates that the *o*-type phase observed in the present study is a

N-enriched non-stoichiometric solid solution with the chemical formula of $Fe_3(N,C)_{1+x}$ ($x < 0.28$). In addition, there is no evidence of back-transformation to the ε-type structure from the o-type phase after quenching at 27 GPa. Both experimental and theoretical results demonstrated that the ε-to-o transition introduces a considerable V reduction (Fig. S10a). The o-type structure should be a high-P phase of the ε-type structure instead of a high-T one. The P of ~27 GPa should be the upper limit of the ε-to-o transition boundary, and ε-type $Fe_7(N_{0.75}C_{0.25})_3$ is metastable in the P of 27~40 GPa and in the T of 450~750 K (Fig. 1).

The h-type phase is experimentally detected above ~40 GPa for either Fe nitride or Fe carbonitride, implying that the incorporation of C in the Fe-N system affects the stability of the h-type phase slightly. In the Fe-C system, Fe_3C melts incongruently to form Fe_7C_3 plus liquid above 10 GPa (Fei and Brosh, 2014). However, Fe_3C is stable over a broad P-T field in the solid state, and decomposes into Fe_7C_3 plus Fe above 145 GPa prior to melting (Liu et al., 2016b). Subsequent experimental studies suggest that Fe_3C and Fe coexist at subsolidus conditions to at least 203 GPa (Mashibo et al., 2019). Although the exact stability field of Fe_3C at multi-megabar pressures remains controversial, previous results support the conclusion that Fe_3C cannot decompose into Fe_7C_3 plus Fe below the solidus at pressures below one megabar, a conclusion also supported by first-principles calculations (Mookherjee et al., 2011). Therefore, the incorporation of N in the Fe-C system can stabilize the h-type phase at high P-T conditions. It is expected that C-rich $Fe_3(C,N)$ is able to dissociate into $Fe_7(C,N)_3$ plus Fe below the solidus at pressures much lower than that for pure Fe_3C.

Three kinds of N-enriched solid solutions, i.e. ε-type, o-type and h-type phases, have been experimentally observed. The V changes caused by the substitution of C for N are small, generally less than 2% in these solid solutions (Fig. 7a and S10a), indicating that the molar volumes of N and C in these structures are very similar. Sokol et al. (2017) found that the solubility of N in o-type Fe_3C is limited to 0.5 wt% at 7.8 GPa, and that the incorporation of 0.5 wt% N leads to a ~10% V expansion. This V change is inconsistent with the present calculations. One possible reason might be that o-type $Fe_3(C,N)_{1+x}$ is unstable on the C-rich side at ambient conditions, and the unit-cell V expands drastically during P quenching. More studies are required to reconcile the discrepancy between experimental and theoretical results. Nevertheless, a large V expansion may be responsible for impeding N solubility in o-type Fe_3C (Sokol et al., 2017). These results may further imply that Fe_3N and Fe_3C cannot form a complete solid solution in the ε-type or o-type phase at low P, since they have distinct crystal structures (Fig. S1). The N-enriched ε-type $Fe_3(N,C)_{1+x}$ transforms into the o-type phase at 26~30 GPa, suggesting a possible complete solid solution at 25~40 GPa across the o-type Fe_3C-Fe_3N join. Similarly, h-type Fe_7C_3 and Fe_7N_3 are likely to form a complete solid solution in the stability field of the h-type phase (i.e. >40 GPa), as observed in diamond inclusions from the lower mantle as well as in our experiments (Kaminsky and Wirth, 2017).

At room T, no structural transition occurs in Fe nitrides or carbonitrides (including cubic γ'-Fe_4N, orthorhombic ζ-Fe_2N and ε-type $Fe_3(N,C)_x$) at pressures up to at least ~70 GPa (Adler and Williams, 2005; Lv et al., 2020; Zhuang et al., 2021). By contrast, previous and present theoretical calculations show that these compounds become unstable at pressures much lower than 70 GPa at 0 K (Niewa et al., 2009b; Schwarz et al., 2009). Indeed, at high temperatures, these compounds transform into high-P polymorphs at significantly lower pressures. For instance, γ'-Fe_4N and ζ-Fe_2N transform into ε-type Fe_4N and Fe_2N at ~10 GPa at high temperatures, respectively (Guo et al., 2013; Schwarz et al., 2009). The ε-type Fe nitrides undergo a reversible structural transition to

the h-type phase above ~40 GPa when laser-annealed (Minobe et al., 2015). The discrepancies between theoretical prediction and experimental observations suggest a kinetic barrier in the structural transitions for Fe nitrides and carbonitrides. This hinders the transformation to high-P phases, and consequently renders the low-P phases metastable to much higher pressures. High T considerably contributes to the rearrangement of atoms to form high-P polymorphs for Fe nitrides and carbonitrides. Based upon our experimental results, the heating T of 750 K is sufficient to overcome the kinetic barrier of the ε-to-h transition for $Fe_7(N_{0.75}C_{0.25})_3$. In the meanwhile, the kinetic barrier of the ε-to-o transition is still unclear. So far, we can only obtain that the kinetic barrier of this transition cannot be overcome by heating to 750 K but can be overcome by heating to ~1200 K.

The ε-to-h structural transition observed in run-3 introduces a ~4% V collapse in $Fe_7(N_{0.75}C_{0.25})_3$ at ~40 GPa (Fig. S10b), which is close to the value (~6%) for pure Fe_7N_3 (Minobe et al., 2015). The V change for Fe_3N or $Fe_3(N_{0.75}C_{0.25})$ is theoretically determined to be ~6% across the ε-to-o structural transition (Fig. S10a). The ε-type structure is derived from a distorted hexagonal close-packed (hcp) structure of Fe. N (or C) atoms occupy the octahedral sites in an ordered or disordered way with many unoccupied vacancies (Niewa et al., 2009a). In o-type and h-type structures, each N (or C) atom is coordinated to six Fe atoms, forming a ditrigonal prism (Fig. S1). The difference in the arrangement of atoms is responsible for a considerable V reduction through the ε-to-o or ε-to-h structural transition. The experimentally determined K_0 of ε-type Fe nitrides and carbonitrides varies from ~130 GPa to ~180 GPa (Table S7) (Adler and Williams, 2005; Litasov et al., 2014, 2017; Lv et al., 2020; Yin et al., 2014). Our experimental and theoretical results suggest that the substitution of C for N has only a slight effect on the compressibility of the ε-type phase (Fig. 5 and Table S4). In contrast, K_0 of the ε-type phase strongly depends on the total concentrations of N and C. With more N and C in the ε-type phase, fewer unoccupied octahedral sites will be present. The NFe_6 (or CFe_6) octahedron is less compressible in comparison to the octahedral vacancy. Therefore, K_0 of the ε-type phase is negatively correlated to the ratio of Fe/(N+C). In terms of the h-type phase, if K_0' is fixed to 3.2 as reported by Chen et al. (2012), the corresponding K_0 are 306(9) GPa, 307 GPa and 316 GPa for $Fe_7(N_{0.75}C_{0.25})_3$, Fe_7C_3 and Fe_7N_3, respectively (Table S9) (Chen et al., 2012; Kusakabe et al., 2019). With a fixed Fe/(N+C) ratio of ~2.33, the K_0 of the h-type phase is nearly independent of the N/C ratio. The thermoelastic parameters of ε-type $Fe_7(N_{0.75}C_{0.25})_3$ obtained in the present study (see Table S7) are similar to those of ε-type $Fe_3N_{0.8}$ and Fe_7N_3 (Litasov et al., 2014, 2017). Moreover, both h-type $Fe_7(N_{0.75}C_{0.25})_3$ and Fe_7C_3 have comparable thermoelastic properties (Lai et al., 2018). To summarize, we suggest that for the Fe-N-C system, the stability and phase transitions of Fe carbonitride at high P-T conditions are mainly controlled by the N/C ratio, with the Fe/(N+C) ratio significantly affecting its isothermal compressibility, whereas the compositional effect plays a negligible role in influencing its thermoelastic parameters (i.e. $\partial K/\partial T$ and α_T).

5 Implications

A recent study has estimated that more than 80% of N in the slab does not return to the surface in the cold slab geotherm (Busigny et al., 2019). Even in the warm slab, about half of N in the slab can be transported to the deep Earth. Potassium silicates, such as cymrite, wadeite and hollandite, are major carriers transporting N in the lithosphere to the lower upper mantle and transition zone via subduction (Sokol et al., 2020; Watenphul et al., 2009). Stishovite, as one of major phases in subducted slabs, is shown to be capable of incorporating a few hundreds of ppm N at 28 GPa and 1700~2000 K, indicating that a large amount of N could have been continuously

transported into the lower mantle to at least ~800 km through subduction (Fukuyama et al., 2020). Recent petrologic observations and mineral physics experiments suggest that native Fe and Fe-enriched alloys may exist not only at the core-mantle boundary (CMB), but also in the bulk deep mantle (Armstrong et al., 2019; Frost et al., 2004; Smith et al., 2016). The Fe-enriched domains in the deep mantle may be alloyed with N throughout geological times, provided that N is continuously supplied by the slabs. The interactions between subducted slabs and Fe-enriched domains can lead to the formation of Fe-N or Fe-N-C compounds during the slab-mantle interaction (Fig. 8). The structures of N-bearing Fe-enriched phases depend on the formation depth and N/C ratios. In general, ε-type and o-type phases are dominant above ~1000 km, and they will both transform into the h-type phase below ~1000 km. Nitrogen is likely to be residing in the deep mantle in the form of Fe nitrides and carbonitrides with diverse polymorphs and compositions. This may keep N hidden from observations at the surface and partially solve the "missing nitrogen" problem. In addition, the Fe-enriched phase can partially or fully melt with the presence of sulfur (S) or nickel (Ni) at the level of several weight percent (Gilfoy and Li, 2020). The solubility of N in the Fe-enriched melt remains nearly unaffected in the metallic melt containing up to ~17 wt% S (Grewal et al., 2019a). Therefore, the Fe-enriched melt can still efficiently extract N from the slabs even when other volatiles are present. Furthermore, there is a large difference in the N bonding between metal alloys (ε-type, o-type and h-type phases) and subducted slabs. The extraction of N from the slabs to the Fe-enriched domains in the bulk mantle is anticipated to be accompanied by considerable N-isotopic fractionations, which can be verified by future studies.
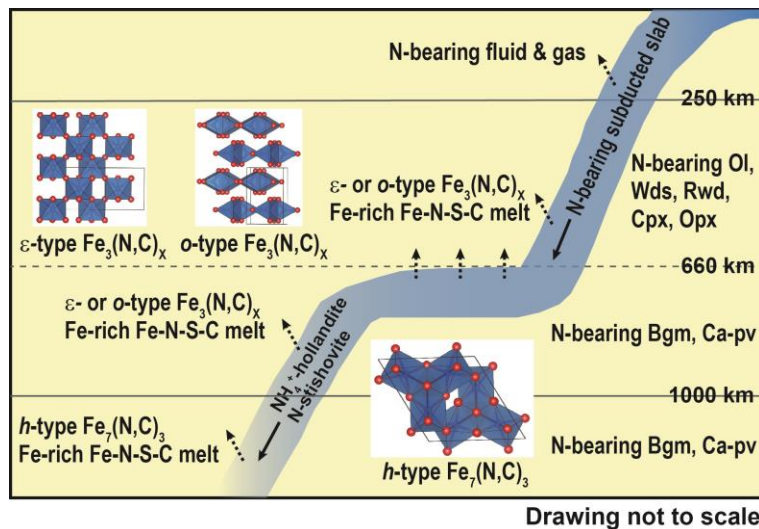
Figure 8 Schematic model for possible N hosts in the deep mantle. The N stored in the mantle can be either from the residue of the primordial mantle or from the injection of N via subducted slabs. Nitrogen can be stored in major silicates of the normal mantle. Below 250 km, where the mantle is saturated with metallic Fe, ε-type and o-type Fe nitrides and carbonitrides become important hosts for N. The h-type Fe nitrides and carbonitrides are energetically favorable in comparison to ε-type and o-type counterparts below 1000 km, and they should be the most significant metallic host for N down to at least 1500 km.

Superdeep diamonds carry unique information about the mineralogy and geochemistry of the inaccessible deep Earth (Kaminsky, 2012). Most superdeep diamonds are typically N-free or

only contain N concentrations at the level of several ppm (Smith et al., 2016). However, recent studies have detected diverse Fe nitrides, carbonitrides, nitrocarbides and carbides as inclusions in lower-mantle diamonds (Kaminsky and Wirth, 2017). The compositions of Fe-N-C inclusions in superdeep diamonds are complex, with the Fe/(N+C) ratio ranging from 1.67 to 3.83 and the N/(N+C) ratio ranging from 0.2 to 0.8. Of particular interest is the fact that Fe_7C_3 and ε-type $Fe_9(N_{0.8}C_{0.2})_4$ coexist as inclusions in a lower-mantle diamond (Kaminsky and Wirth, 2017). Based on the compositional and structural analysis of two inclusions and the phase relation of the Fe-C system at high pressures, Kaminsky and Wirth (2017) suggested that the observed Fe alloys probably originated from the CMB after migrating from the Earth's liquid outer core. Although Fe and Fe_7C_3 become eutectic at very high pressures, Fe_7C_3 can be formed by the incongruent melting of Fe_3C above ~10 GPa (Fei and Brosh, 2014; Liu et al., 2016b). In addition, Fe_7C_3 can occur as an intermediate by-product of the reaction between metallic Fe and subducted carbonates (Zhu et al., 2019a). This assemblage likely represent reduced domains in the lower mantle, which can be locally preserved throughout the mantle and contribute to the primordial redox heterogeneity of the mantle. However, the occurrence of this assemblage as inclusions may not necessarily indicate a CMB origin (Zedgenizov and Litasov, 2017). Another possibility is that this assemblage is formed through a two-stage crystallization process involving a Fe-N-C melt in the so-called metallic pockets in the deep mantle (Smith et al. 2016). Fe_7C_3 has the highest melting temperature among Fe carbides and nitrides, and it will crystallize first from the melt (Kusakabe et al., 2019; Liu et al., 2016b). However, the TEM image showing Fe_7C_3 transects $Fe_9(N_{0.8}C_{0.2})_4$ indicates that $Fe_9(N_{0.8}C_{0.2})_4$ is formed no later than Fe_7C_3. In addition, this model cannot explain why Fe_7C_3 coexisting with N-rich $Fe_9(N_{0.8}C_{0.2})_4$ is totally N-free, unless N only partitions into metallic melt when in equilibrium with Fe_7C_3. This explanation is contradicted by the observation of a $Fe_7(C_{0.73}N_{0.27})_3$ inclusion in a diamond from the lower mantle (Kaminsky and Wirth, 2017).

Based on our results, we propose that the origin of this assemblage is an h-type N-enriched $Fe_7(N,C)_3$ precursor phase. When h-type $Fe_7(N,C)_3$ is carried into shallow regions, it will transform into the low-P ε-type phase as observed in the present study. The incorporation of C in the ε-type phase has an upper limit that is controlled by P and T (Sokol et al., 2017). This phase transformation will be accompanied by the exsolution of Fe_7C_3, which can be described as h-type $Fe_7(N_{1-m}C_m)_3 \rightarrow \varepsilon$-type $Fe_7(N_{1-n}C_n)_3 + Fe_7C_3$ ($m > n$); this possibility is supported by the fact that Fe_7C_3 and ε-type $Fe_9(N_{0.8}C_{0.2})_4$ have similar Fe/(C+N) ratios (Kaminsky and Wirth, 2017). The N-enriched $Fe_7(N,C)_3$ precursor can either be the residue of the primordial mantle or be formed by the interaction between subducted slabs and Fe-enriched domains in the lower mantle. The isotopic characteristics of inclusions in superdeep diamonds can in principle place additional constraints on the origin of these light elements (Dalou et al., 2019). On the other hand, the o-type Fe carbonitride or nitrocarbide has not been found in superdeep diamonds yet. The o-type phase observed in the present study can be T-quenched, but it remains unclear whether or not it is quenchable to ambient P. Further investigations are required to constrain the stability field of the o-type phase as a function of its N/C ratios. In addition to silicates and oxides, the structural and compositional features of Fe-N-C inclusions as a function of P, T and even redox conditions can also shed light on the depth of formation of superdeep diamonds and geodynamic processes in the lower mantle.

Recent studies have proposed that the Earth's inner core can consist predominantly of h-type Fe_7C_3 or Fe_7N_3 because their densities can match the density of the inner core (Chen et al., 2012; Kusakabe et al., 2019). The h-type $Fe_7(C,N)_3$ is also suggested to be a candidate constituent of the inner core under the assumption that its two endmembers could form a continuous solid

solution at high *P-T* conditions (Kusakabe et al., 2019; Minobe et al., 2015). Our study provides the first experimental confirmation of the existence of an *h*-type Fe_7C_3-Fe_7N_3 solid solution above 40 GPa. We also find that the substitution of C for N slightly affects the compressibility and thermoelastic properties of Fe-N-C compounds with a fixed Fe/(N+C) ratio. It is expected that the density of an intermediate *h*-type $Fe_7(C,N)_3$ phase, such as $Fe_7(N_{0.75}C_{0.25})_3$ in the present study, will be very close to that of its two endmembers when extrapolated to much higher *P-T* conditions. On the other hand, a recent theoretical study has predicted a new monoclinic high-*P* phase for Fe_7N_3 and Fe_7C_3 above ~250 GPa (Sagatov et al., 2019). Subsequent simulations suggested that Fe_7C_3 might decompose into the mixture of Fe_2C and Fe_3C at conditions of the Earth's inner core (Sagatov et al., 2020). Whether these results could be applied in the Fe-N-C ternary system is still under debate. More experimental and theoretical studies are required to determine the phase stability, density and physical properties of *h*-type $Fe_7(C,N)_3$ solid solutions at simultaneous high *P-T* conditions relevant to the Earth's core, which can offer more clues to decipher the Earth's core compositions and the speciation of N in the Earth's core.

References

Adler, J. F., & Williams, Q. (2005). A high-pressure X-ray diffraction study of iron nitrides: Implications for Earth's core. *Journal of Geophysical Research: Solid Earth*, *110*, B01203. https://doi.org/10.1029/2004JB003103

Angel, R. J., Alvaro, M., & Gonzalez-Platas, J. (2014). EosFit7c and a Fortran module (library) for equation of state calculations. *Zeitschrift für Kristallographie*, *229*(5), 405-419. https://doi.org/10.1515/zkri-2013-1711

Armstrong, K., Frost, D. J., McCammon, C. A., Rubie, D. C., & Ballaran, T. B. (2019). Deep magma ocean formation set the oxidation state of Earth's mantle. *Science*, *365*(6456), 903-906. https://doi.org/10.1126/science.aax8376

Bergin, E. A., Blake, G. A., Ciesla, F., Hirschmann, M. M., & Li, J. (2015). Tracing the ingredients for a habitable earth from interstellar space through planet formation. *Proceedings of the National Academy of Sciences*, *112*(29), 8965-8970. https://doi.org/10.1073/pnas.1500954112

Berman, R. G. (1988). Internally-consistent thermodynamic data for minerals in the system Na_2O-K_2O-CaO-MgO-FeO-Fe_2O_3-Al_2O_3-SiO_2-TiO_2-H_2O-CO_2. *Journal of Petrology*, *29*(2), 445-522. https://doi.org/10.1093/petrology/29.2.445

Birch, F. (1947). Finite elastic strain of cubic crystals. *Physical Review*, *71*(11), 809-824. https://doi.org/10.1103/PhysRev.71.809

Busigny, V., Cartigny, P., Laverne, C., Teagle, D., Bonifacie, M., & Agrinier, P. (2019). A re-assessment of the nitrogen geochemical behavior in upper oceanic crust from Hole 504B: Implications for subduction budget in Central America. *Earth and Planetary Science Letters*, *525*, 115735. https://doi.org/10.1016/j.epsl.2019.115735

Campbell, A. J., Danielson, L., Righter, K., Seagle, C. T., Wang, Y., & Prakapenka, V. B. (2009). High pressure effects on the iron-iron oxide and nickel-nickel oxide oxygen fugacity buffers. *Earth and Planetary Science Letters*, *286*, 556-564. https://doi.org/10.1016/j.epsl.2009.07.022

Chen, B., Gao, L., Lavina, B., Dera, P., Alp, E. E., Zhao, J., & Li, J. (2012). Magneto-elastic coupling in compressed Fe_7C_3 supports carbon in Earth's inner core. *Geophysical Research Letters*, *39*(18), L18301. https://doi.org/10.1029/2012GL052875

Chen, B., Li, Z., Zhang, D., Liu, J., Hu, M. Y., Zhao, J., Bi, W., Alp, E. E., Xiao, Y., Chow, P., & Li, J. (2014). Hidden carbon in Earth's inner core revealed by shear softening in dense Fe_7C_3. *Proceedings of the National Academy of Sciences*, *111*(50), 17,755-17,758. https://doi.org/10.1073/pnas.1411154111

Chen, B., Lai, X., Li, J., Liu, J., Zhao, J., Bi, W., Alp, E. E., Hu, M. Y., & Xiao, Y. (2018). Experimental constrains on the sound velocities of cementite Fe_3C to core pressures. *Earth and Planetary Science Letters*, *494*, 164-171. https://doi.org/10.1016/j.epsl.2018.05.002

Dalou, C., Hirschmann, M. M., von der Handt, A., Mosenfelder, J., & Armstrong, L. S. (2017). Nitrogen and carbon fractionation during core-mantle differentiation at shallow depth. *Earth and Planetary Science Letters*, *458*, 141-151. https://doi.org/10.1016/j.epsl.2016.10.026

Dalou, C., Füri, E., Deligny, C., Piani, L., Caumon, M. C., Laumonier, M., Boulliung, J., & Edén, M. (2019). Redox control on nitrogen isotope fractionation during planetary core formation. *Proceedings of the National Academy of Sciences*, *116*(29), 14485-14494. https://doi.org/10.1073/pnas.1820719116

Fei, Y., & Brosh, E. (2014). Experimental study and thermodynamic calculations of phase relations in the Fe-C system at high pressure. *Earth and Planetary Science Letters*, *408*, 155-162. https://doi.org/10.1016/j.epsl.2014.09.044

Fei, Y., Ricolleau, A., Frank, M., Mibe, K., Shen, G., & Prakapenka, V. (2007). Toward an internally consistent pressure scale. *Proceedings of the National Academy of Sciences*, *104*(22), 9182-9186. https://doi.org/10.1073/pnas.0609013104
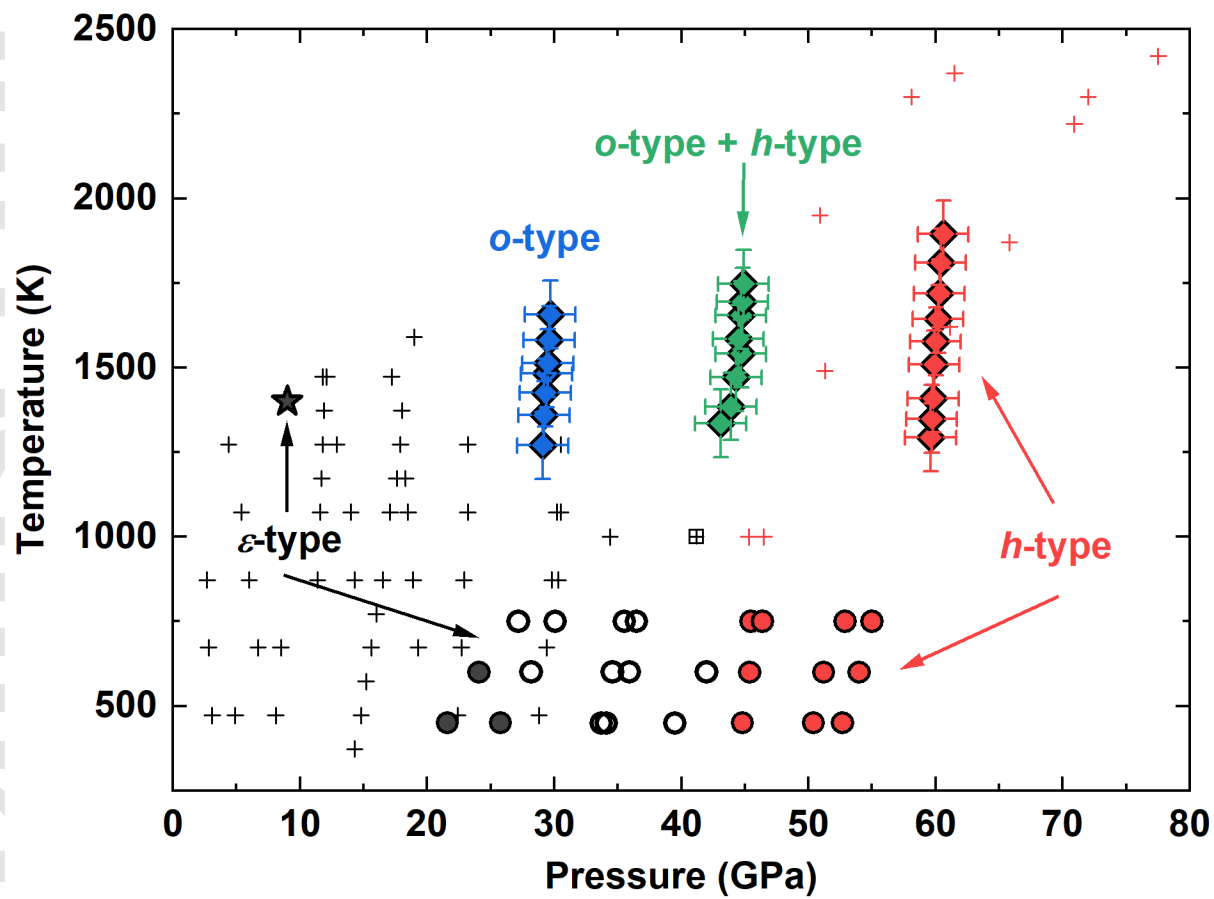
Frost, D. J., Liebske, C., Langenhorst, F., McCammon, C. A., Trønnes, R. G., & Rubie, D. C. (2004). Experimental evidence for the existence of iron-rich metal in the Earth's lower mantle. *Nature*, *428*(6981), 409-412. https://doi.org/10.1038/nature02413

Fukuyama, K., Kagi, H., Inoue, T., Kakizawa, S., Shinmei, T., Hishita, S., Takahata, N., & Sano, Y. (2020). High nitrogen solubility in stishovite (SiO_2) under lower mantle conditions. *Scientific Reports*, *10*, 10897. https://doi.org/10.1038/s41598-020-67621-2

Gilfoy, F., & Li, J. (2020). Thermal state and solidification regime of the martian core: Insights from the melting behavior of FeNi-S at 20 GPa. *Earth and Planetary Science Letters*, *541*, 116285. https://doi.org/10.1016/j.epsl.2020.116285

Grewal, D. S., Dasgupta, R., Holmes, A. K., Costin, G., Li, Y., & Tsuno, K. (2019a). The fate of nitrogen during core-mantle separation on Earth. *Geochimica et Cosmochimica Acta*, *251*, 87-115. https://doi.org/10.1016/j.gca.2019.02.009

Grewal, D. S., Dasgupta, R., Sun, C., Tsuno, K., & Costin, G. (2019b). Delivery of carbon, nitrogen, and sulfur to the silicate Earth by a giant impact. *Science Advances*, *5*(1), eaau3669. https://doi.org/10.1126/sciadv.aau3669

Guo, K., Rau, D., von Appen, J., Prots, Y., Schnelle, W., Dronskowski, R., Niewa, R., & Schwarz, U. (2013). High pressure high-temperature behavior and magnetic properties of Fe_4N: experiment and theory. *High Pressure Research*, *33*(3), 684-696. https://doi.org/10.1080/08957959.2013.809715

Johnson, B., & Goldblatt, C. (2015). The nitrogen budget of Earth. *Earth-Science Reviews*, *148*, 150-173. https://doi.org/10.1016/j.earscirev.2015.05.006

Kaminsky, F. (2012). Mineralogy of the lower mantle: A review of 'super-deep' mineral inclusions in diamond. *Earth-Science Reviews*, *110*, 127-147. https://doi.org/10.1016/j.earscirev.2011.10005

Kaminsky, F., & Wirth, R. (2017). Nitrides and carbonitrides from the lowermost mantle and their importance in the search for Earth's "lost" nitrogen. *American Mineralogist*, *102*(8), 1667-1676. https://doi.org/10.2138/am-2017-6101

Kresse, G., & Joubert, D. (1999). From ultrasoft pseudopotentials to the projector augmented-wave method. *Physical Review B*, *59*(3), 1758-1775. https://doi.org/10.1103/PhysRevB.59.1758

Kusakabe, M., Hirose, K., Sinmyo, R., Kuwayama, Y., Ohishi, Y., & Helffrich, G. (2019). Melting curve and equation of state of β-Fe_7N_3: Nitrogen in the core? *Journal of Geophysical Research: Solid Earth*, *124*(4), 3448-3457. https://doi.org/10.1029/2018JB015823

Lai, X., Zhu, F., Liu, J., Zhang, D., Hu, Y., Finkelstein, G. J., Dera, P., & Chen, B. (2018). The high-pressure anisotropic thermoelastic properties of a potential inner core carbon-bearing phase, Fe_7C_3, by single-crystal X-ray diffraction. *American Mineralogist*, *103*(10), 1568-1574. https://doi.org/10.2138/am-2018-6527

Lai, X., Zhu, F., Zhang, J. S., Zhang, D., Tkachev, S., Prakapenka, V. B., & Chen, B. (2020). An externally-heated diamond anvil cell for synthesis and single-crystal elasticity determination of ice-VII at high pressure-temperature conditions. *Journal of Visualized Experiments*, *160*, e61389. https://doi.org/10.3791/61389

Lei, L., Zhang, L., Gao, S., Hu, Q., Fang, L., Chen, X., et al. (2018). Neutron diffraction study of the structural and magnetic properties of ε-$Fe_3N_{1.098}$ and ε-$Fe_{2.322}Co_{0.678}N_{0.888}$. *Journal of Alloys and Compounds*, *752*, 99-105. https://doi.org/10.1016/j.jallcom.2018.04.143

Leinenweber, K., Tyburczy, J. A., Sharp, T., Soignard, E., Diedrich, T., Petuskey, W. B., Wang, Y., & Mosenfelder, J. (2012). Cell assemblies for reproducible multi-anvil experiments (the
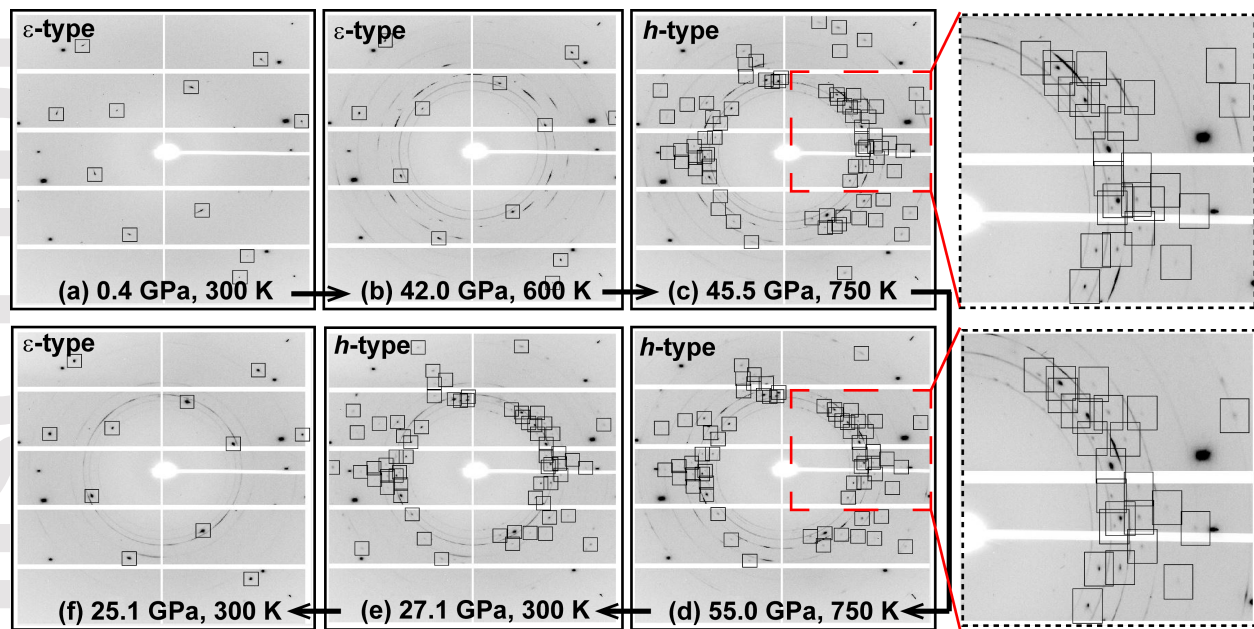
COMPRES assemblies). *American Mineralogist*, *97*, 353-368. https://doi.org/10.2138/am.2012.3844

Litasov, K. D., Shatskiy, A. F., Ovchinnikov, S. G., Popov, Z. I., Ponomarev, D. S., & Ohtani, E. (2014). Phase transformations of iron nitrides Fe_3N-Fe_4N studied by in situ X-ray diffractions. *JETP Letters*, *98*(12), 805-808. https://doi.org/10.1134/S0021364013250140

Litasov, K. D., Popov, Z. I., Gavryushkin, P. N., Ovchinnikov, S. G., & Fedorov, A. S. (2015). First-principles calculations of the equations of state and relative stability of iron carbides at the Earth's core pressures. *Russian Geology and Geophysics*, *56*(1-2), 164-171. https://doi.org/10.1016/j.rgg.2015.01.010

Litasov, K. D., Shatskiy, A. F., & Ohtani, E. (2016). Interaction of Fe and Fe_3C with hydrogen and nitrogen at 6–20 GPa: a study by in situ X-ray diffraction. *Geochemistry International*, *54*(10), 914-921. https://doi.org/10.1134/S0016702916100074

Litasov, K. D., Shatskiy, A., Ponomarev, D. S., & Gavryushkin, P. N. (2017). Equations of state of iron nitrides ε-Fe_3N_x and γ-Fe_4N_y to 30 GPa and 1200 K and implication for nitrogen in the Earth's core. *Journal of Geophysical Research: Solid Earth*, *122*(5), 3574-3584. https://doi.org/10.1002/2017JB014059

Liu, J., Li, J., & Ikuta, D. (2016a). Elastic softening in Fe_7C_3 with implications for Earth's deep carbon reservoirs. *Journal of Geophysical Research: Solid Earth*, *121*(3), 1514-1524. https://doi.org/10.1002/2015JB012701

Liu, J., Lin, J. F., Prakapenka, V. B., Prescher, C., & Yoshino, T. (2016b). Phase relations of Fe_3C and Fe_7C_3 up to 185 GPa and 5200 K: Implication for the stability of iron carbide in the Earth's core. *Geophysical Research Letters*, *43*(24), 12415-12422. https://doi.org/10.1002/2016GL071353

Liu, Y., Li, H., Lai, X., Zhu, F., Rapp, R. P., & Chen, B. (2020). Casting octahedra for reproducible multi-anvil experiments by 3D-printed molds. *Minerals*, *10*, 4. https://doi.org/10.3390/min10010004

Lv, M., Liu, J., Zhu, F., Li, J., Zhang, D., Xiao, Y., & Dorfman, S. M. (2020). Spin transitions and compressibility of ε-Fe_7N_3 and γ'-Fe_4N: Implications for iron alloys in terrestrial planet cores. *Journal of Geophysical Research: Solid Earth*, *124*, e2020JB020660. https://doi.org/10.1029/2020JB020660

Marty, B. (2012). The origins and concentrations of water, carbon, nitrogen and noble gases on Earth. *Earth and Planetary Science Letters*, *313*, 56-66. https://doi.org/10.1016/j.epsl.2011.10.040

Mashino, I., Miozzi, F., Hirose, K., Morard, G., & Sinmyo, R. (2019). Melting experiments on the Fe-C binary system up to 255 GPa: Constraints on the carbon content in the Earth's core. *Earth and Planetary Science Letters*, *515*, 135-144. https://doi.org/10.1016/j.epsl.2019.03.020

Mikhail, S., & Sverjensky, D. A. (2014). Nitrogen speciation in upper mantle fluids and the origin of Earth's nitrogen-rich atmosphere. *Nature Geoscience*, *7*(11), 816-819. https://doi.org/10.1038/ngeo2271

Minobe, S., Nakajima, Y., Hirose, K., & Ohishi, Y. (2015). Stability and compressibility of a new iron-nitride β-Fe_7N_3 to core pressures. *Geophysical Research Letters*, *42*(13), 5206-5211. https://doi.org/10.1002/2015GL064496
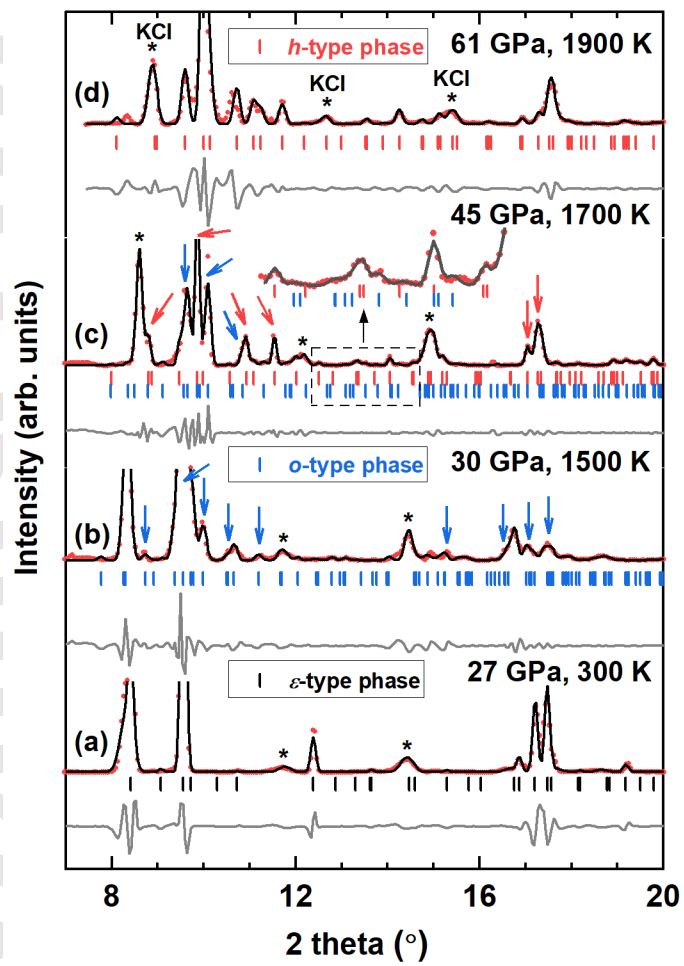
Mookherjee, M., Nakajima, Y., Steinle-Neumann, G., Glazyrin, K., Wu, X., Dubrovinsky, L., McCammon, C., & Chumakov, A. (2011). High-pressure behavior of iron carbide (Fe_7C_3) at inner core conditions. *Journal of Geophysical Research: Solid Earth*, *116*(B4), B04201. https://doi.org/10.1029/2010JB007819

Murnaghan, F. D. (1944). The compressibility of media under extreme pressures. *Proceedings of the National Academy of Sciences*, *30*(9), 244-247. https://doi.org/10.1073/pnas.30.9.244

Nakajima, Y., Takahashi, E., Sata, N., Nishihara, Y., Hirose, K., Funakoshi, K. I., & Ohishi, Y. (2011). Thermoelastic property and high-pressure stability of Fe_7C_3: Implication for iron-carbide in the Earth's core. *American Mineralogist*, *96*(7), 1158-1165. https://doi.org/10.2138/am.2011.3703

Niewa, R., Rau, D., Wosylus, A., Meier, K., Hanfland, M., Wessel, M., Dronskowski, R., Dzivenko, D. A., Riedel, R., & Schwarz, U. (2009a). High-pressure, high-temperature single-crystal growth, ab initio electronic structure calculations, and equation of state of ε-Fe_3N_{1+x}. *Chemistry of Materials*, *21*(2), 392-398. https://doi.org/10.1021/cm802721k

Niewa, R., Rau, D., Wosylus, A., Meier, K., Wessel, M., Hanfland, M., Dronskowski, R., & Schwarz, U. (2009b). High-pressure high-temperature phase transition of γ'-Fe_4N. *Journal of Alloys and Compounds*, *480*(1), 76-80. https://doi.org/10.1016/j.jallcom.2008.09.178

Perdew, J. P., Burke, K., & Ernzerhof, M. (1996). Generalized gradient approximation made simple. *Physical Review Letters*, *77*(18), 3865-3868. https://doi.org/10.1103/PhysRevLett.77.3865

Popov, Z. I., Litasov, K. D., Gavryushkin, P. N., Ovchinnikov, S., & Fedorov, A. S. (2015). Theoretical study of γ'-Fe_4N and ε-Fe_xN iron nitrides at pressures up to 500 GPa. *JETP Letters*, *101*(6), 371-375. https://doi.org/10.1134/S0021364015060090

Prescher, C., Dubrovinsky, L., McCammon, C., Glazyrin, K., Nakajima, Y., Kantor, A., Merlini, M., & Hanfland, M. (2012). Structurally hidden magnetic transitions in Fe_3C at high pressures. *Physical Review B*, *85*(14), 140402. https://doi.org/10.1103/PhysRevB.85.140402

Roskosz, M., Bouhifd, M. A., Jephcoat, A. P., Marty, B., & Mysen, B. O. (2013). Nitrogen solubility in molten metal and silicate at high pressure and temperature. *Geochimica et Cosmochimica Acta*, *121*, 15-28. https://doi.org/10.1016/j.gca.2013.07.007

Sagatov, N., Gavryushkin, P. N., Inerbaev, T. M., & Litasov, K. D. (2019). New high-pressure phases of Fe_7N_3 and Fe_7C_3 stable at Earth's core conditions: evidences for carbon-nitrogen isomorphism in Fe-compounds. *RSC Advances*, *9*(7), 3577-3581. https://doi.org/10.1039/C8RA09942A

Sagatov, N. E., Gavryushkin, P. N., Medrish, I. V., Inerbaev, T. M., & Litasov, K. D. (2020). Phase relations of iron carbides Fe_2C, Fe_3C, and Fe_7C_3 at the Earth's core pressures and temperatures. *Russian Geology and Geophysics*, *61*(12), 1345-1353. https://doi.org/10.15372/RGG2019146

Schwarz, U., Wosylus, A., Wessel, M., Dronskowski, R., Hanfland, M., Rau, D., & Niewa, R. (2009). High-pressure-high-temperature behavior of ζ-Fe_2N and phase transition to ε-$Fe_3N_{1.5}$. *European Journal of Inorganic Chemistry*, *2009*(12), 1634-1639. https://doi.org/10.1002/ejic.200801222

Smith, E. M., Shirey, S. B., Nestola, F., Bullock, E. S., Wang, J., Richardson, S. H., & Wang, W. (2016). Large gem diamonds from metallic liquid in Earth's deep mantle. *Science*, *354*(6318), 1403-1405. https://doi.org/10.1126/science.aal1303

Sokol, A. G., Kruk, A. N., Seryotkin, Y. V., Korablin, A. A., & Palyanov, Y. N. (2017). Phase relations in the Fe-Fe_3C-Fe_3N system at 7.8 GPa and 1350° C: Implications for carbon and

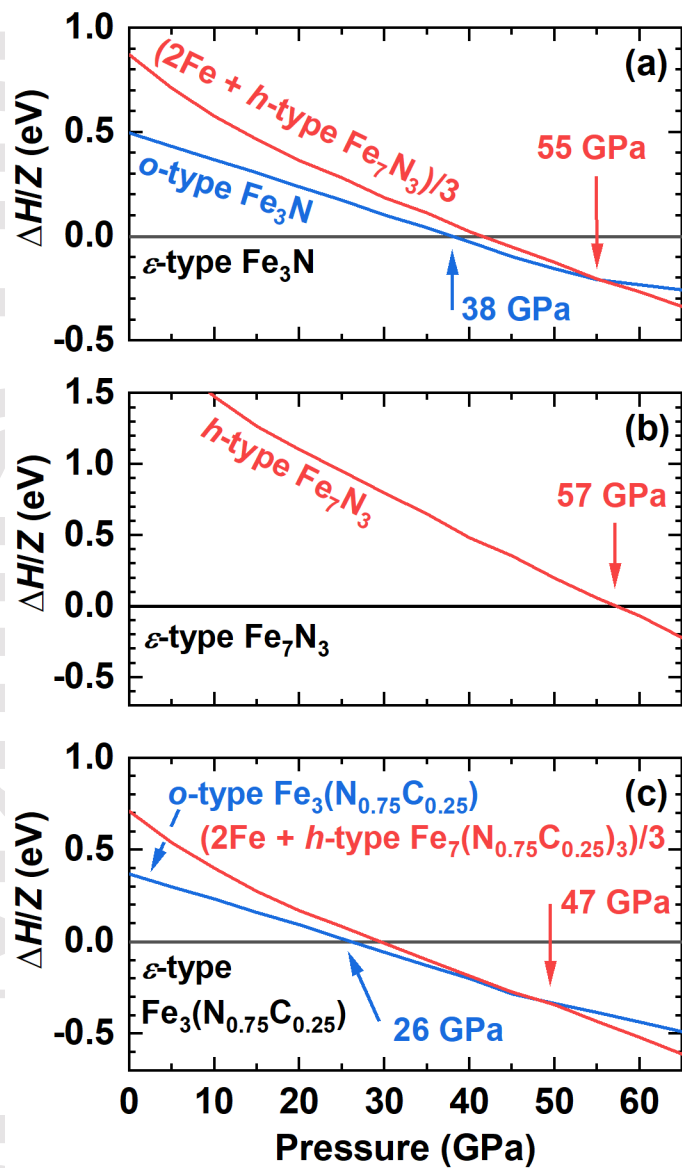nitrogen hosts in Fe^0-saturated upper mantle. *Physics of the Earth and Planetary Interiors*, *265*, 43-53. https://doi.org/10.1016/j.pepi.2017.02.007

Sokol, A. G., Kupriyanov, I. N., Seryotkin, Y. V., Sokol, E. V., Kruk, A. N., Tomilenko, A. A., Bul'bak, T. A., & Palyanov, Y. N. (2020). Cymrite as mineral clathrate: An overlooked redox insensitive transporter of nitrogen in the mantle. *Gondwana Research*, *79*, 70-86. https://doi.org/10.1016/j.gr.2019.08.013

Tateno, S., Komabayashi, T., Hirose, K., Hirao, N., & Ohishi, Y. (2019). Static compression of B2 KCl to 230 GPa and its PVT equation of state. *American Mineralogist*, *104*(5), 718-723. https://doi.org/10.2138/am-2019-6779

von der Handt, A., & Dalou, C. (2016). Quantitative EPMA of nitrogen in silicate glasses. *Microscopy and Microanalysis*, *22*(S3), 1810-1811. https://doi.org/10.1017/S1431927616009892

Walker, D., Dasgupta, R., Li, J., & Buono, A. (2013). Nonstoichiometry and growth of some Fe carbides. *Contributions to Mineralogy and Petrology*, *166*(3), 935-957. https://doi.org/10.1007/s00410-013-0900-7

Walker, D., Li, J., Kalkan, B., & Clark, S. M. (2015). Thermal, compositional, and compressional demagnetization of cementite. *American Mineralogist*, *100*(11-12), 2610-2624. https://doi.org/10.2138/am-2015-5306

Watenphul, A., Wunder, B., & Heinrich, W. (2009). High-pressure ammonium-bearing silicates: Implications for nitrogen and hydrogen storage in the Earth's mantle. *American Mineralogist*, *94*(2-3), 283-292. https://doi.org/10.2138/am.2009.2995

Wriedt, H., Gokcen, N., & Nafziger, R. (1987). The Fe-N (iron-nitrogen) system. *Bulletin of Alloy Phase Diagrams*, *8*(4), 355-377.

Yin, W., Lei, L., Jiang, X., Liu, P., Liu, F., Li, Y., Peng, F., & He, D. (2014). High pressure synthesis and properties studies on spherical bulk ϵ-Fe$_3$N. *High Pressure Research*, *34*(3), 317-326. https://doi.org/10.1080/08957959.2014.944910

Yoshioka, T., Wiedenbeck, M., Shcheka, S., & Keppler, H. (2018). Nitrogen solubility in the deep mantle and the origin of Earth's primordial nitrogen budget. *Earth and Planetary Science Letters*, *488*, 134-143. https://doi.org/10.1016/j.epsl.2018.02.021

Zedgenizov, D. A., & Litasov, K. D. (2017). Looking for "missing" nitrogen in the deep Earth. *American Mineralogist*, *102*(9), 1769-1770. https://doi.org/10.2138/am-2017-6218

Zhu, F., Li, J., Liu, J., Lai, X., Chen, B., & Meng, Y. (2019a). Kinetic control on the depth distribution of superdeep diamonds. *Geophysical Research Letters*, *46*(4), 1984-1992. https://doi.org/10.1029/2018GL080740

Zhu, F., Li, J., Walker, D., Liu, J., Lai, X., & Zhang, D. (2019b). Origin and consequences of non-stoichiometry in iron carbide Fe$_7$C$_3$. *American Mineralogist*, *104*(3), 325-332. https://doi.org/10.2138/am-2019-6672

Zhuang, Y., Su, X., Salke, N. P., Cui, Z., Hu, Q., Zhang, D., & Liu, J. (2021). The effect of nitrogen on the compressibility and conductivity of iron at high pressure. *Geoscience Frontiers*, *12*(2), 983-989. https://doi.org/10.1016/j.gsf.2020.04.012

(a) 0.4 GPa, 300 K

(b) 42.0 GPa, 600 K

(c) 45.5 GPa, 750 K

(d) 55.0 GPa, 750 K

(e) 27.1 GPa, 300 K

(f) 25.1 GPa, 300 K

ε-type

ε-type

h-type

ε-type

h-type

h-type

(a)

(b)

Legend (a):
- h-Fe$_7$N$_3$, M2015
- h-Fe$_7$C$_3$, C2012
- h-Fe$_7$C$_3$, L2016
- h-Fe$_7$C$_3$, N2011

h-Fe$_7$(N$_{0.75}$C$_{0.25}$)$_3$
- run3, comp.
- run3, decomp.
- run4

Legend (b):
- run3, 300 K, comp.
- run3, 300 K, decomp.
- run4, 300 K
- run3, 450 K
- run3, 600 K
- run3, 750 K

Volume (Å^3)

Pressure (GPa)

N-bearing fluid & gas

N-bearing subducted slab

250 km

ε-type Fe$_3$(N,C)$_X$ o-type Fe$_3$(N,C)$_X$

ε- or o-type Fe$_3$(N,C)$_X$
Fe-rich Fe-N-S-C melt

N-bearing Ol,
Wds, Rwd,
Cpx, Opx

660 km

ε- or o-type Fe$_3$(N,C)$_X$
Fe-rich Fe-N-S-C melt

NH$_4^+$-hollandite
N-stishovite

N-bearing Bgm, Ca-pv

1000 km

h-type Fe$_7$(N,C)$_3$
Fe-rich Fe-N-S-C melt

h-type Fe$_7$(N,C)$_3$

N-bearing Bgm, Ca-pv

Drawing not to scale

High-pressure phase stability and thermoelastic properties of iron carbonitrides and nitrogen in the deep Earth

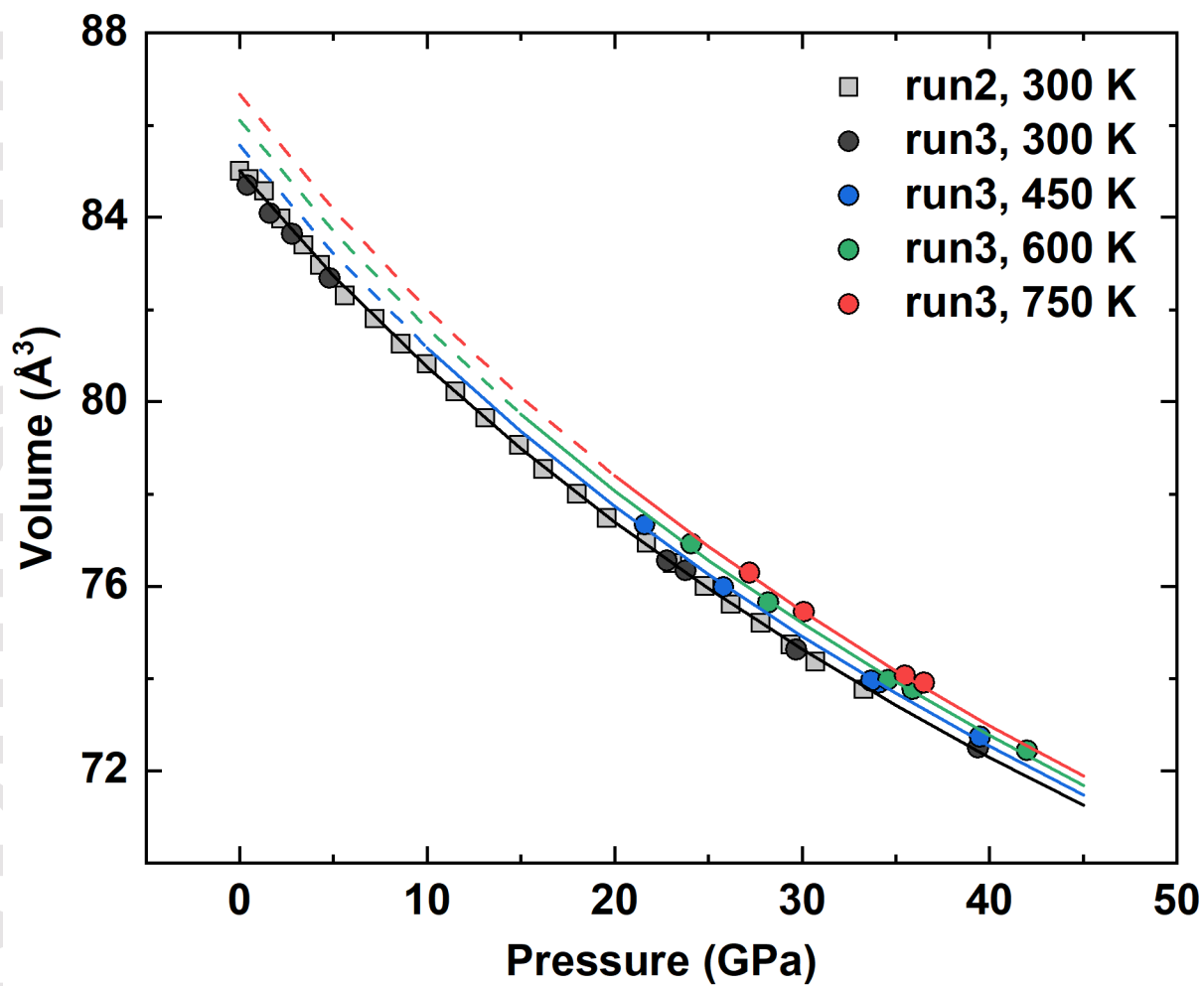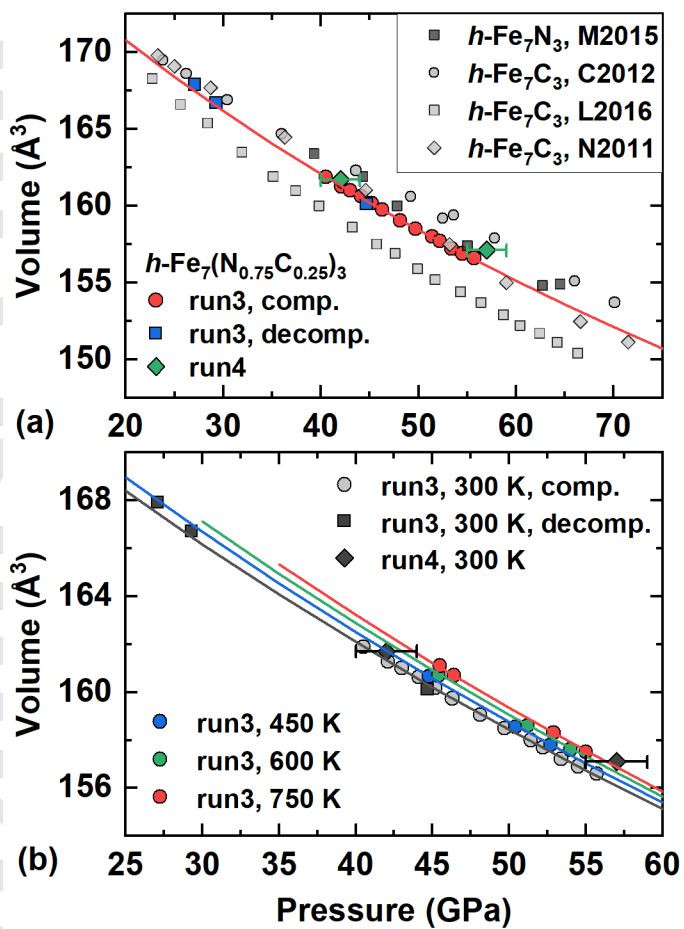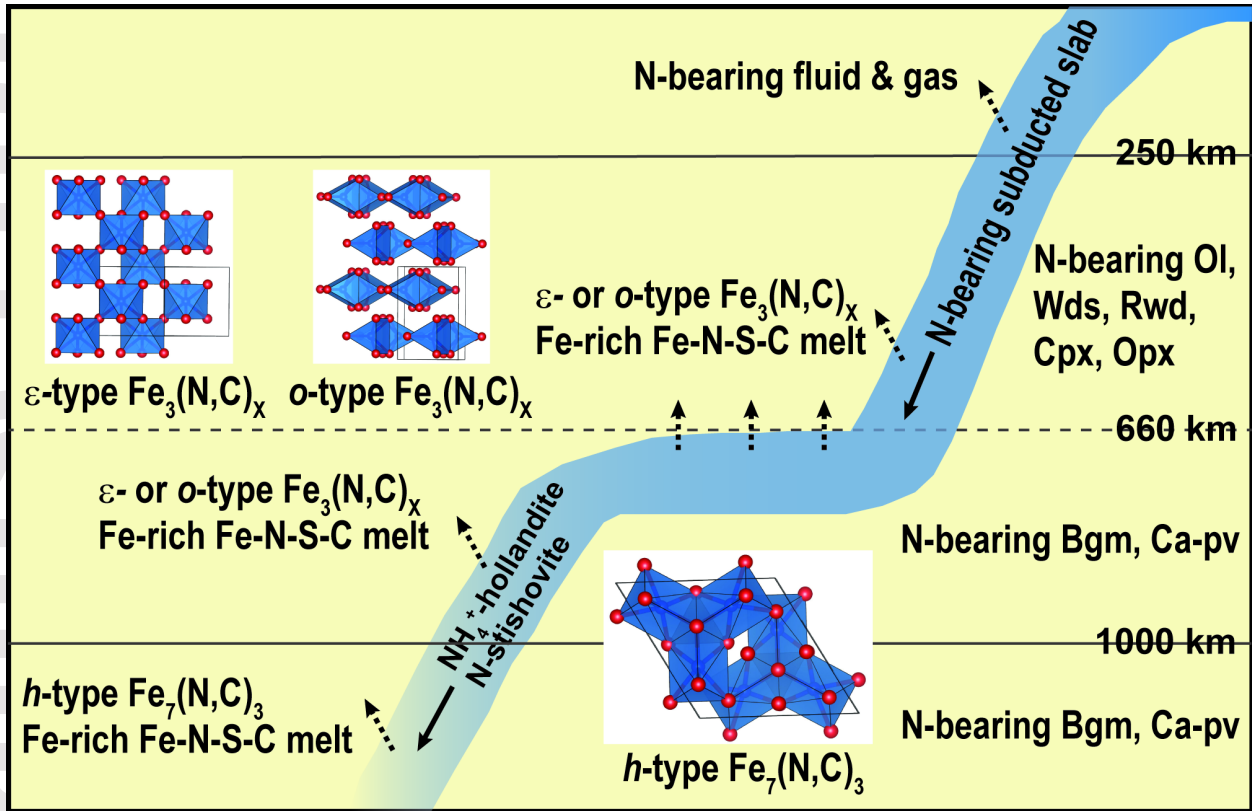Shengxuan Huang[1,2,3], Xiang Wu[3], Feng Zhu[2], Xiaojing Lai[4], Jie Li[5], Owen K. Neill[5], Shan Qin[1], Robert Rapp[2], Dongzhou Zhang[2,6], Przemyslaw Dera[2], Stella Chariton[6], Vitali B. Prakapenka[6], and Bin Chen[2]

[1]Key Laboratory of Orogenic Belts and Crustal Evolution, MOE, Peking University and School of Earth and Space Sciences, Peking University, Beijing, China

[2]Hawai'i Institute of Geophysics and Planetology, University of Hawai'i at Mānoa, Honolulu, HI, USA

[3]State key laboratory of geological processes and mineral resources, China University of Geosciences, Wuhan, China

[4]Gemmological Institute, China University of Geosciences, Wuhan, China

[5]Department of Earth and Environmental Sciences, University of Michigan, Ann Arbor, MI, USA

[6]Center for Advanced Radiation Sources, University of Chicago, Chicago, IL, USA

Contents of this file

Figures S1 to S14
Tables S1 to S9
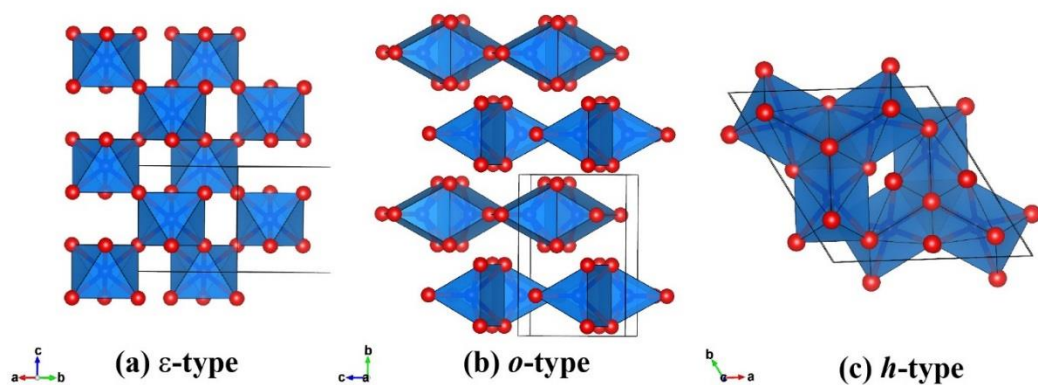
Figure S1. Crystal structures of (a) ε-type ($P3_12$), (b) o-type (Fe$_3$C-type, *Pnma*) and (c) *h*-type (Fe$_7$C$_3$-type, $P6_3mc$) phases. Red and blue spheres represent Fe and N (or C) atoms, respectively.
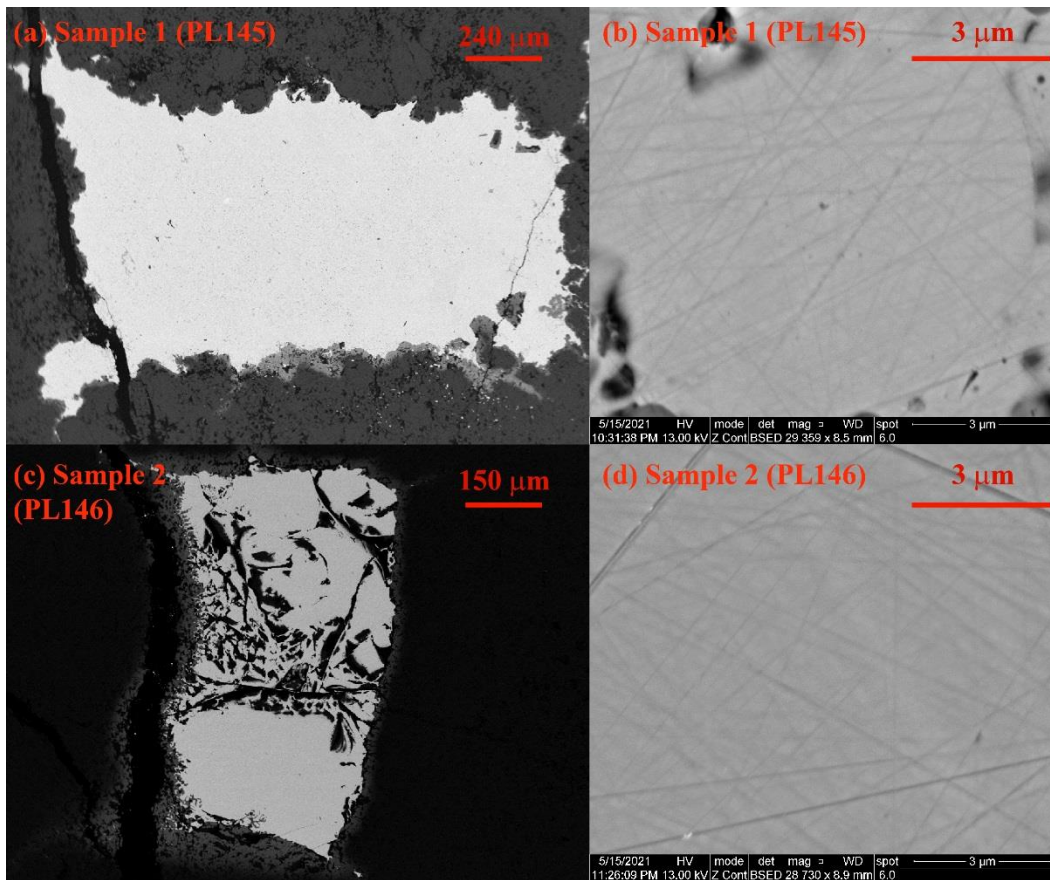
Figure S2. Back-scattered electron (BSE) images of two synthetic samples. Parts of the second sample were poked to collect grains for synchrotron-based experiments, causing some cracks as showed in (c).
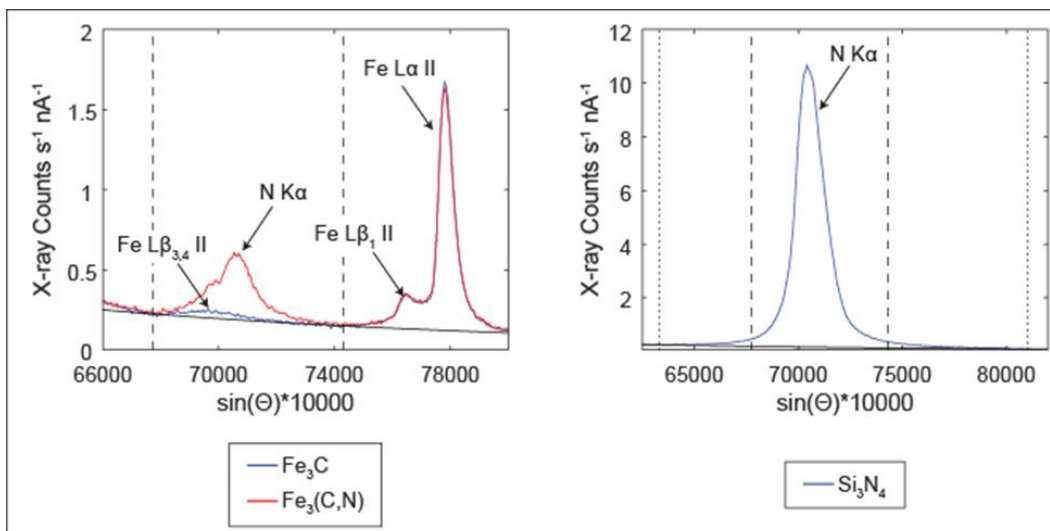
Figure S3. Wavelength scans around the N Kα peak position on pure, N-free Fe₃C (left, blue line), a mixed Fe-N-C sample (left, red line), and pure Si₃N₄ (right). Dashed lines indicated off-peak positions used to measure continuum in Fe-N-C samples, dotted lines indicate off-peak positions used for measurements of the Si₃N₄ standard. Solid black lines indicated continuum intensities modeled from off-peak measurements, used to estimate continuum intensity at the N Kα peak position.
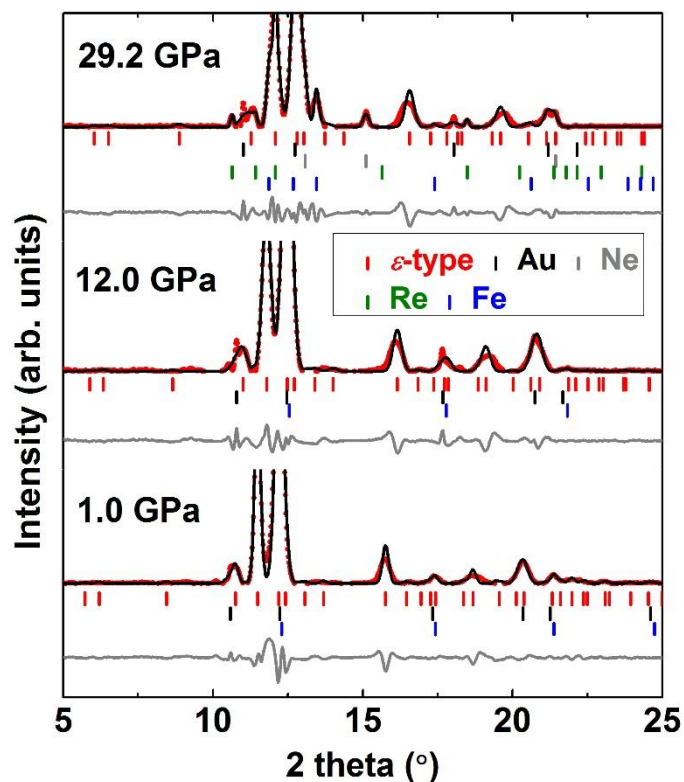
Figure S4. The representative fitting results of XRD patterns for ε-type $Fe_4(N_{0.6}C_{0.4})$ at different pressures at room *T* in run-1 by the Le Bail method. Backgrounds are subtracted from the original data. Measured (red circles), calculated (black continuous line) intensities and the difference curve (grey continuous line) between observed and calculated spectra are shown respectively. The red, black, blue, green and grey ticks represent Bragg peaks of the ε-type phase, Au, Fe, Re and Ne, respectively.
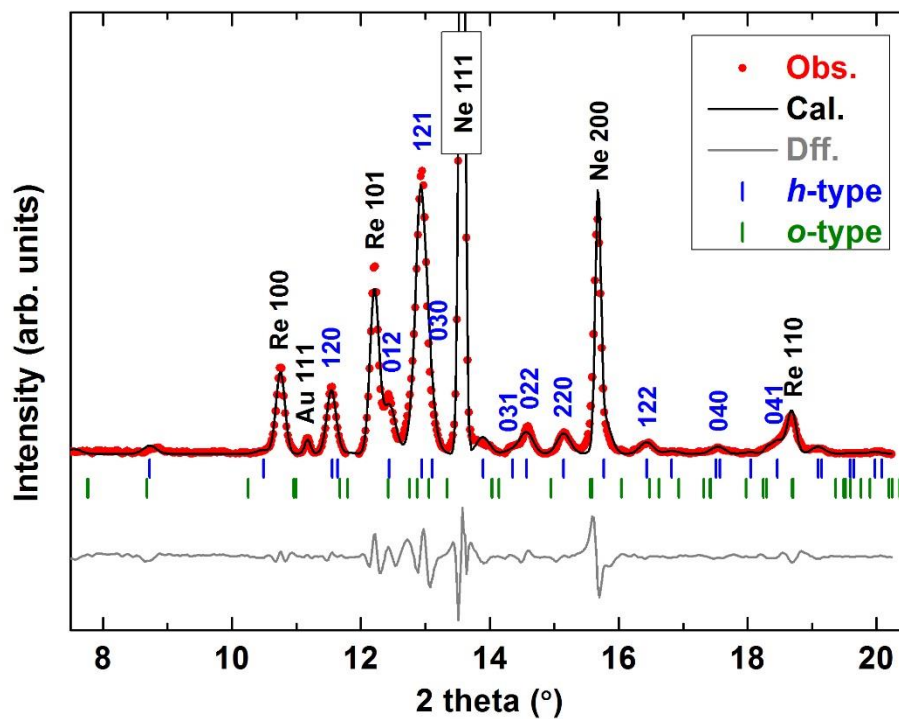
Figure S5. Le Bail fit of an XRD spectrum of the *h*-type $Fe_7(N_{0.75}C_{0.25})_3$ at 44.1 GPa and room *T* in run-3. Backgrounds are subtracted from the original data. Measured (red circles), calculated (black continuous line) intensities and the difference curve (grey continuous line) between observed and calculated spectra are shown respectively. The blue and green ticks represent Bragg peaks of the *h*-type and *o*-type phases, respectively.
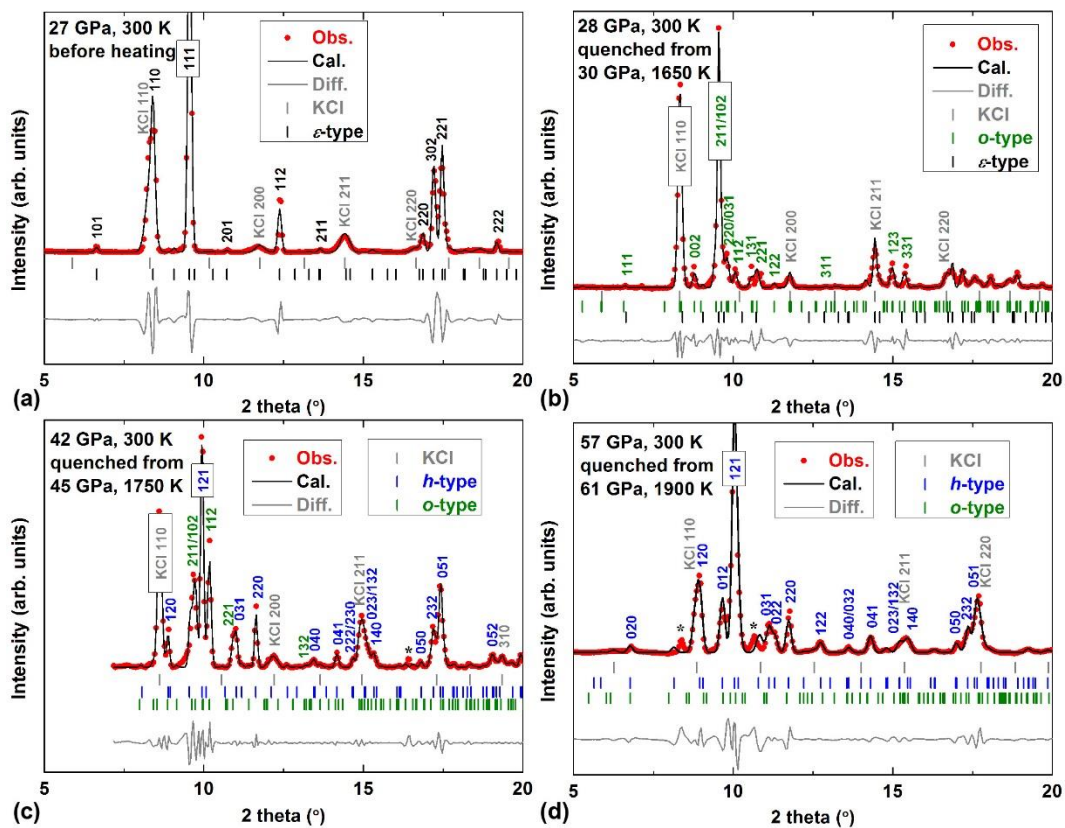
Figure S6. The representative fitting results of XRD patterns for $Fe_7(N_{0.75}C_{0.25})_3$ at different pressures after quenching in run-4 by the Le Bail method. Backgrounds are subtracted from the original data. Measured (red circles), calculated (black continuous line) intensities and the difference curve (grey continuous line) between observed and calculated spectra are shown respectively. The grey, black, green, and blue ticks represent Bragg peaks of KCl, ε-type, o-type, and h-type phases, respectively.
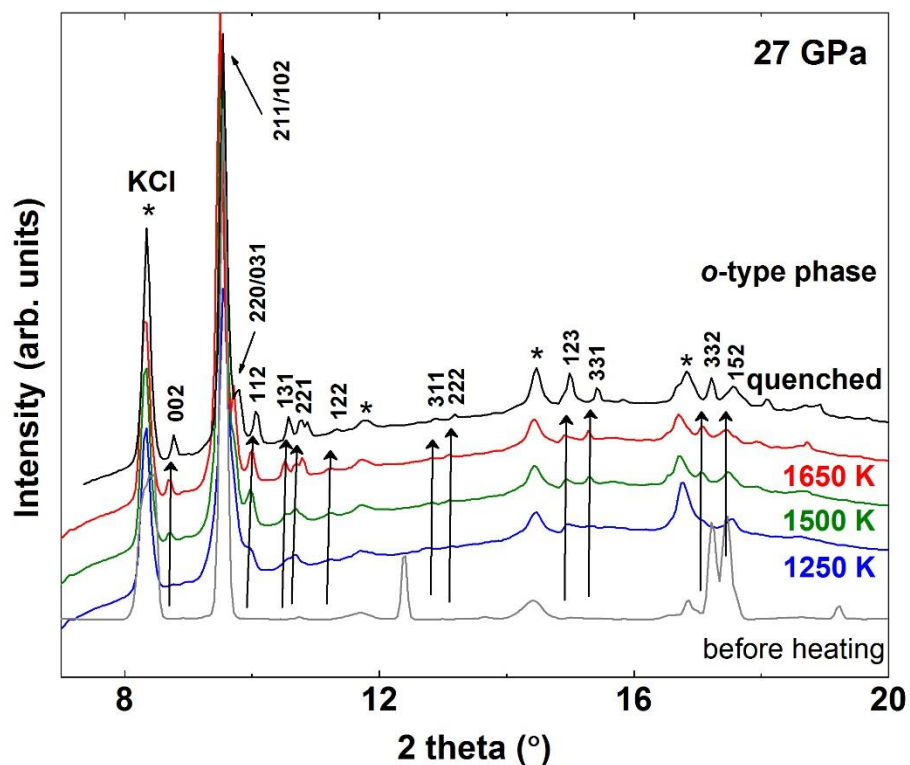
Figure S7. Full XRD patterns before, during and after heating at ~27 GPa. The arrows indicate the emergence and growth of Bragg peaks of the *o*-type phase upon heating.
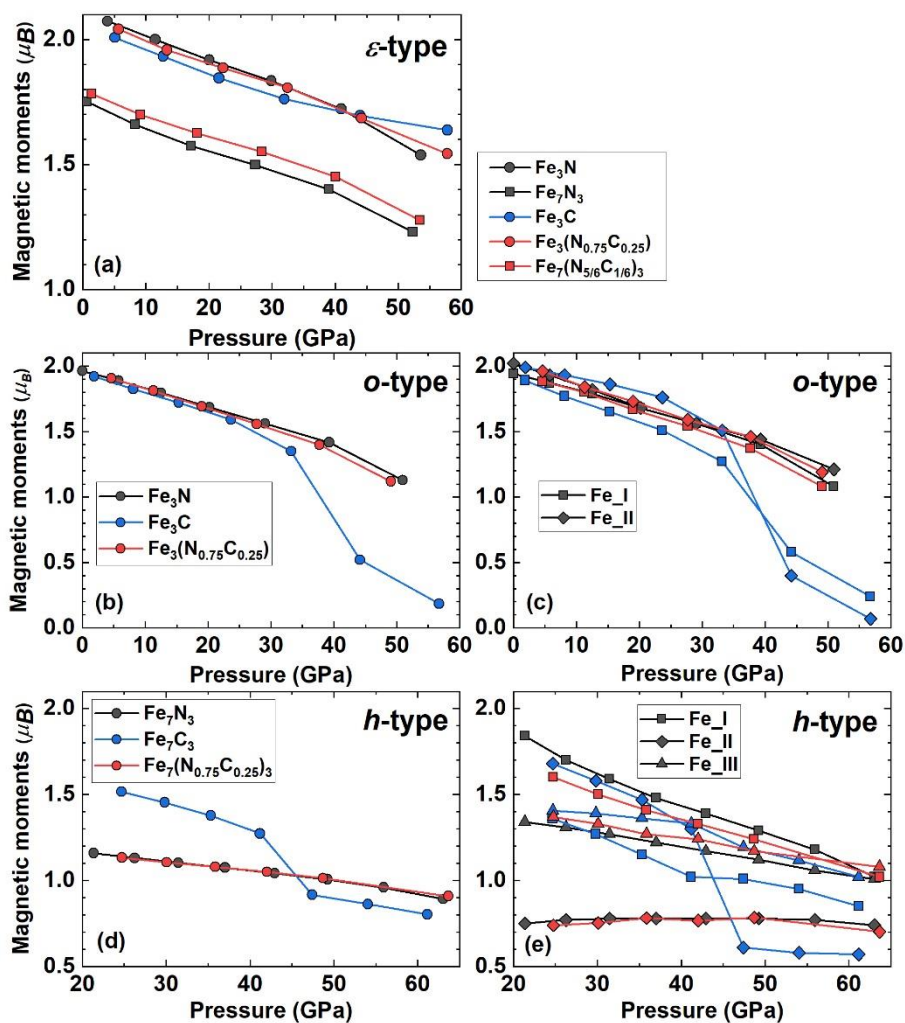
Figure S8 Evolution of average magnetic moments (a), (b) and (d) and sub-lattice magnetic moments (c) and (e) of each calculated phase as a function of *P*.
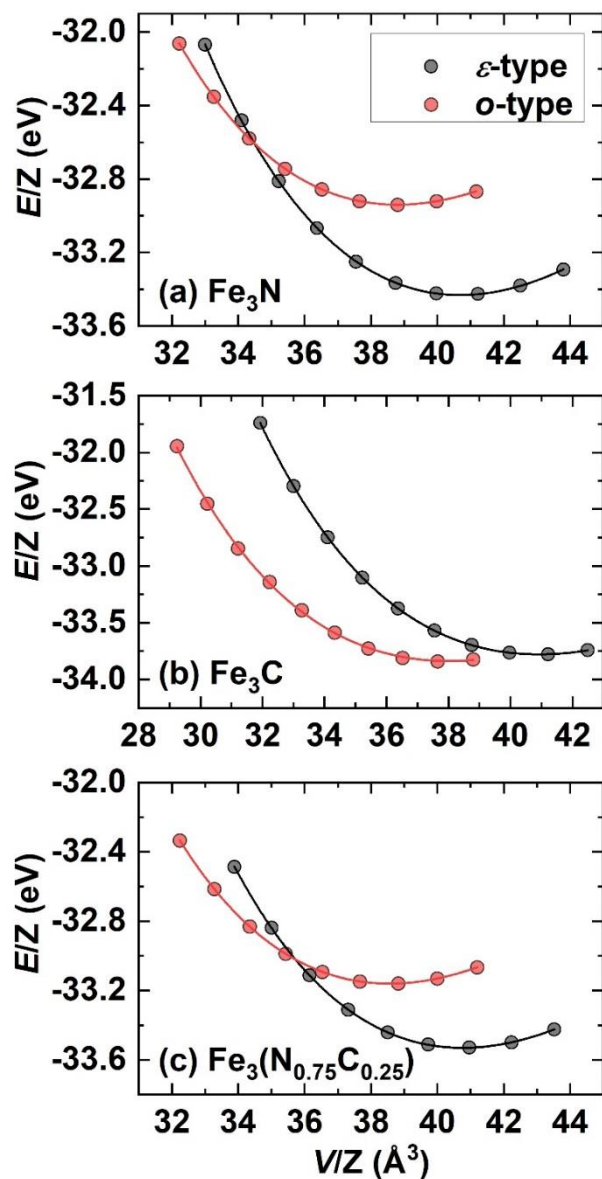
Figure S9. *V-E* curves of (a) Fe_3N, (b) Fe_3C and (c) $Fe_3(N_{0.75}C_{0.25})$ with different structures. Fe_3N and $Fe_3(N_{0.75}C_{0.25})$ are predicted to transform from the ε-type phase into the o-type phase at 38 GPa and 26 GPa at 0 K, respectively. The o-type Fe_3C is energetically favorable in comparison with its ε-type counterpart over the calculated *V* (or *P*) range.
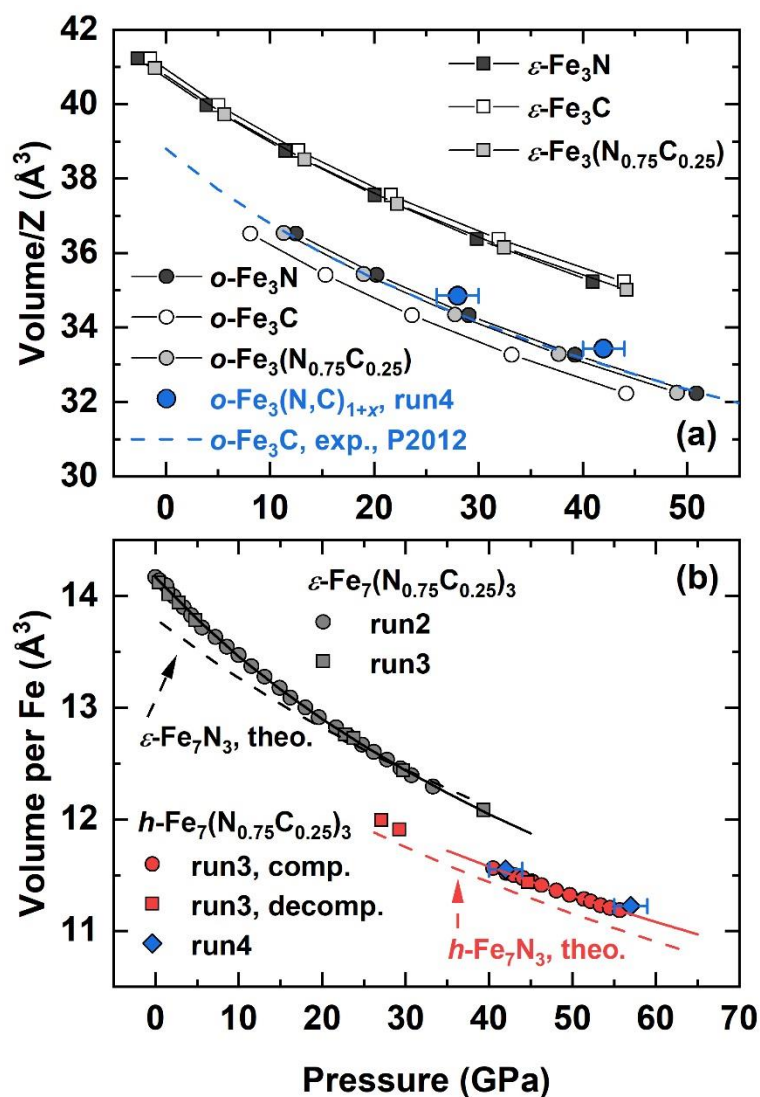
Figure S10. Calculated *P-V* curves of Fe_3N, Fe_3C and $Fe_3(N_{0.75}C_{0.25})$ with different structures (a). Experimental and calculated *P-V* curves of ε-type and *h*-type $Fe_7(N_{0.75}C_{0.25})_3$ (b). Previous experimental data of *o*-type Fe_3C are plotted for comparison (Prescher et al., 2012).
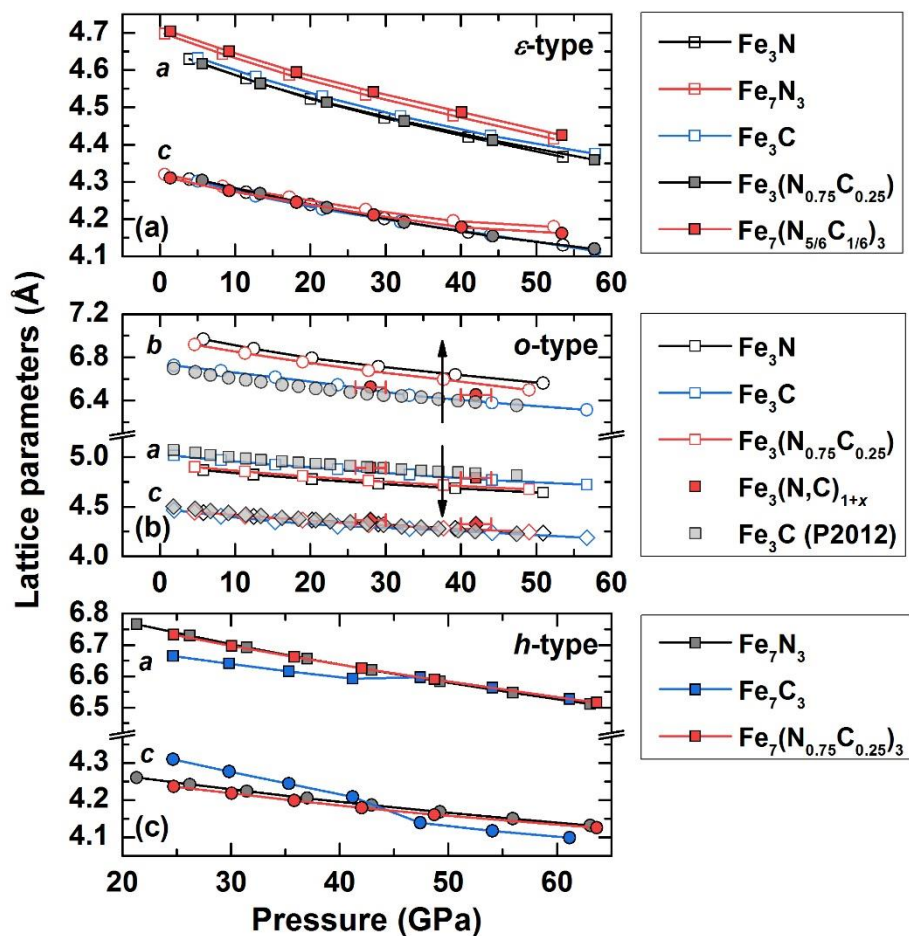
Figure S11. Evolution of lattice parameters of each calculated phase as a function of *P*. Previous experimental data of *o*-type Fe₃C are plotted for comparison (Prescher et al., 2012).
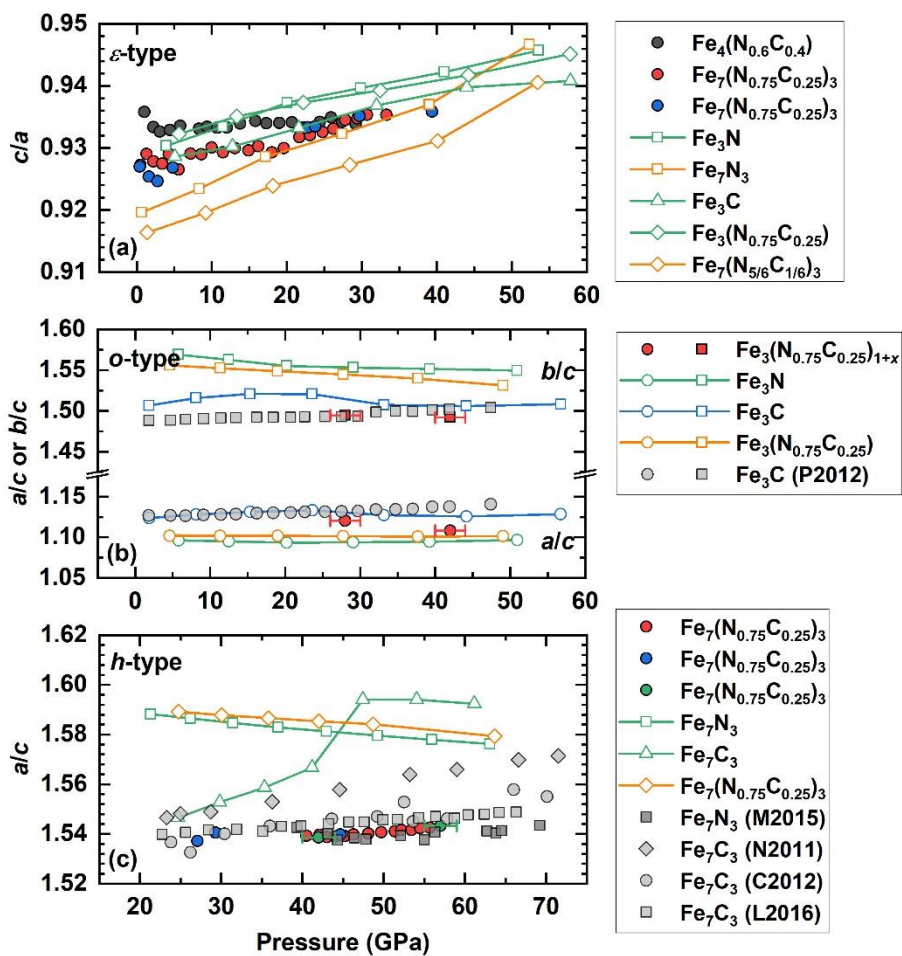
Figure S12. Evolution of axial ratios of each phase as a function of *P* from experiments (solid marks) and calculations (open marks). Previous experimental data of *o*-type Fe_3C (Prescher et al., 2012) as well as *h*-type Fe_7N_3 and Fe_7C_3 (Chen et al., 2012; Liu et al., 2016a; Minobe et al., 2015; Nakajima et al., 2011) are plotted for comparison.
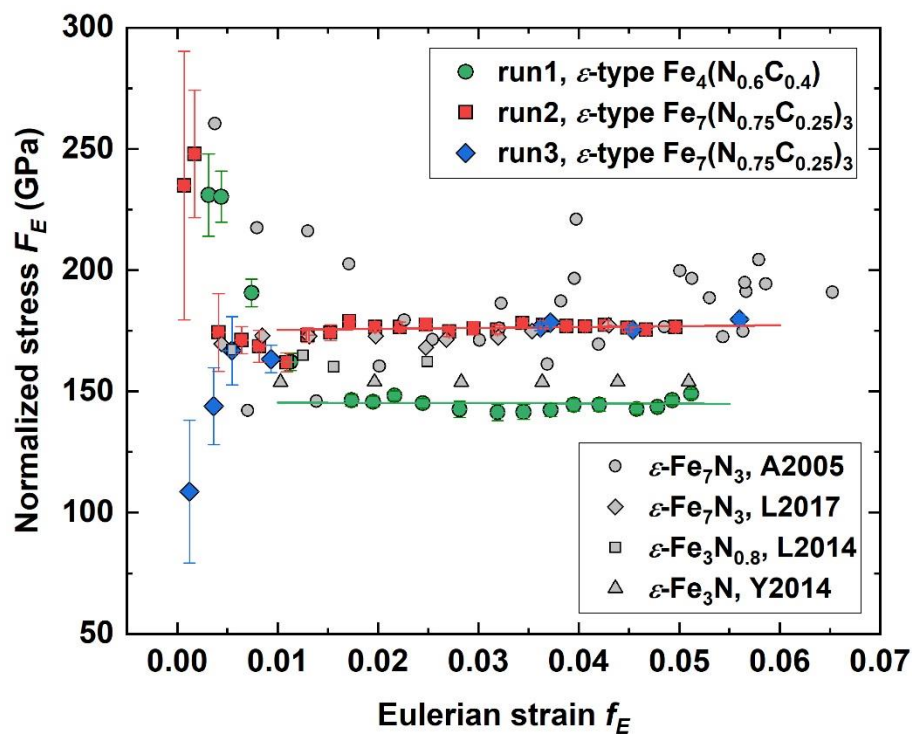
Figure S13. The Eulerian strain-normalized stress (f_E-F_E) plot of the unit-cell V of ε-type $Fe_4(N_{0.6}C_{0.4})$ (green circles) and $Fe_7(N_{0.75}C_{0.25})_3$ (red and blue circles). The green solid line is obtained by the linear fitting using data with $f_E > 0.012$ in run-1. The red solid line is obtained by the linear fitting using data with $f_E > 0.012$ in run-2 and run-3. Previous experimental data of ε-type Fe nitrides are plotted for comparison (Adler and Williams, 2005; Litasov et al., 2014, 2017; Yin et al., 2014).
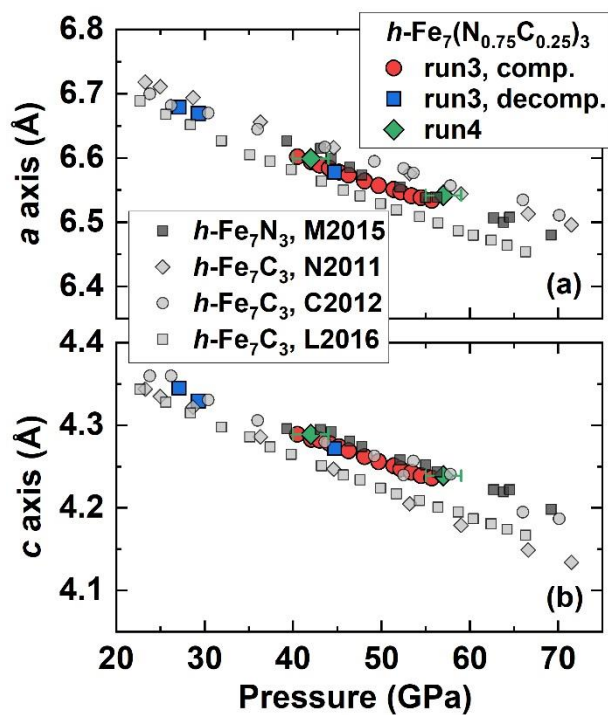
Figure S14. Evolution of lattice parameters of the *h*-type Fe$_7$(N$_{0.75}$C$_{0.25}$)$_3$ as a function of *P* in run-3 and run-4. Previous experimental data of *h*-type Fe$_7$N$_3$ and Fe$_7$C$_3$ are plotted for comparison (Chen et al., 2012; Liu et al., 2016a; Minobe et al., 2015; Nakajima et al., 2011).

Table S1 EPMA results for two synthetic Fe carbonitrides. AE represents "Analytical error".

No.	Fe (wt%)	N (wt%)	C (wt%)	Total (wt%)	Fe (at%)	N (at%)	C (at%)	AE Fe (%)	AE N (%)	AE C (%)
Sample 1 (PL145, $Fe_4(N_{0.6}C_{0.4})$)										
8-63	93.9	3.7	1.7	99.3	80.6	12.5	6.9	0.13	1.39	0.88
8-64	93.2	3.5	2.0	98.7	80.1	12.0	7.9	0.13	1.42	0.81
8-66	93.8	3.6	1.9	99.3	80.3	12.1	7.5	0.13	1.40	0.83
8-67	94.0	3.7	1.8	99.5	80.3	12.7	7.0	0.13	1.37	0.87
8-70	93.7	3.1	2.0	98.8	81.1	10.8	8.1	0.13	1.52	0.80
8-71	93.7	3.2	2.1	98.9	80.7	11.0	8.3	0.13	1.51	0.79
8-74	94.2	3.2	2.2	99.5	80.6	10.9	8.6	0.13	1.51	0.77
8-75	93.9	3.2	2.1	99.2	80.7	11.0	8.4	0.13	1.50	0.79
8-76	93.6	3.1	2.0	98.7	81.3	10.7	8.0	0.13	1.54	0.81
8-77	93.8	3.1	2.0	98.9	81.2	10.8	8.0	0.13	1.54	0.81
8-80	93.4	3.2	2.0	98.5	81.0	11.0	8.0	0.13	1.52	0.81
8-81	94.0	3.3	2.0	99.3	80.6	11.3	8.0	0.13	1.48	0.81
8-82	93.3	3.6	2.1	99.0	79.6	12.1	8.3	0.13	1.42	0.79
Ave	93.7	3.3	2.0	99.0	80.6	11.5	7.9	0.13	1.47	0.81
Sample 2 (PL146, $Fe_7(N_{0.75}C_{0.25})_3$)										
9-83	90.1	7.1	2.1	99.3	70.2	22.1	7.8	0.14	0.95	0.77
9-84	90.3	7.1	2.1	99.5	70.3	22.0	7.7	0.14	0.95	0.77
9-85	90.5	7.4	2.1	99.9	69.8	22.7	7.5	0.14	0.92	0.78
9-86	90.1	7.2	2.1	99.4	69.9	22.4	7.7	0.14	0.94	0.76
9-87	89.9	7.3	2.1	99.3	69.9	22.5	7.6	0.14	0.94	0.78
9-88	90.3	7.4	2.0	99.8	69.9	22.8	7.3	0.14	0.93	0.79
9-89	89.9	7.2	2.0	99.2	70.1	22.5	7.4	0.14	0.94	0.79
9-90	90.3	7.2	2.1	99.7	70.1	22.3	7.6	0.14	0.94	0.77
9-91	90.2	7.3	2.1	99.6	69.9	22.4	7.7	0.14	0.93	0.77
9-92	90.3	7.0	2.2	99.5	70.3	21.8	7.9	0.14	0.95	0.76
9-93	90.7	7.4	2.1	100.1	69.8	22.6	7.6	0.14	0.92	0.77
9-94	90.6	7.4	2.1	100.0	69.9	22.7	7.4	0.14	0.93	0.78
9-95	90.4	7.5	2.1	100.0	69.4	23.0	7.6	0.14	0.92	0.77
9-96	90.4	7.4	2.2	100.0	69.5	22.7	7.8	0.14	0.93	0.76
9-97	90.5	7.2	2.1	99.8	70.2	22.3	7.4	0.14	0.94	0.79
9-98	90.8	7.3	2.1	100.2	70.0	22.6	7.4	0.14	0.93	0.78
9-99	90.6	7.3	2.1	100.0	69.9	22.3	7.7	0.14	0.94	0.77
9-100	90.9	7.5	2.2	100.6	69.3	22.8	7.9	0.14	0.92	0.75
9-101	90.3	7.1	2.1	99.6	70.2	22.1	7.7	0.14	0.95	0.77
9-102	90.2	7.1	2.1	99.4	70.3	22.1	7.6	0.14	0.94	0.78
Ave	90.4	7.3	2.1	99.8	69.9	22.4	7.6	0.14	0.94	0.77

Table S2 Summary of details of diamond anvil cell experiments.

Runs	Samples	Conditions	Techniques	Beamline
1	$Fe_4(N_{0.6}C_{0.4})$	to 60 GPa at 300 K	DAC	13-BMC
2	$Fe_7(N_{0.75}C_{0.25})_3$	to 50 GPa at 300 K	DAC	13-BMC
3	$Fe_7(N_{0.75}C_{0.25})_3$	to 55 GPa and 750 K	EHDAC	13-BMC
4	$Fe_7(N_{0.75}C_{0.25})_3$	to 61 GPa and 1900 K	LHDAC	13-IDD

Table S3 Observed and calculated d-spacings of h-type ($P6_3mc$) $Fe_7(N_{0.75}C_{0.25})_3$ at 44.1 GPa and 300 K. The refined lattice parameters of h-type $Fe_7(N_{0.75}C_{0.25})_3$ are V = 160.62(9) Å^3, a = 6.584(1) Å, c = 4.278(2) Å.

hkl	d_{obs} (Å)	d_{cal} (Å)	Δd (Å)
120	2.1562	2.1551	0.0011
012	2.0040	2.0029	0.0011
121	1.9257	1.9247	0.0010
030	1.9009	1.9007	0.0002
031	1.7360	1.7370	-0.0010
022	1.7100	1.7111	-0.0011
122	1.5170	1.5182	-0.0012
040	1.4245	1.4255	-0.0010
041	1.3523	1.3524	-0.0001

Table S4 Calculated EoS parameters of Fe nitrides, carbides and carbonitrides at 0 K. The ε-type, o-type and h-type represent the $P3_12$, $Pnma$ (Fe_3C-type) and $P6_3mc$ (Fe_7C_3-type) structures, respectively. All candidate phases listed below are in the ferromagnetic state except Fe, for which the stable phase is converged to the non-magnetic state at high P after structural relaxations.

Phase	E_0/Z (eV)	V_0/Z ($Å^3$)	K_0 (GPa)	K_0'
ε-type Fe_3N	-33.43	40.7	213	4.02
ε-type Fe_7N_3	-35.73	41.4	231	4.33
o-type Fe_3N	-32.94	38.8	180	4.53
h-type Fe_7N_3	-81.66	91.3	230	4.13
ε-type Fe_3C	-33.78	40.9	205	4.80
o-type Fe_3C	-33.84	38.0	183	4.53
h-type Fe_7C_3	-84.86	90.6	229	4.22
ε-type $Fe_3(N_{0.75}C_{0.25})$	-33.53	40.8	206	4.50
ε-type $Fe_7(N_{5/6}C_{1/6})_3$	-35.87	41.5	232	4.21
o-type $Fe_3(N_{0.75}C_{0.25})$	-33.16	38.6	188	4.22
h-type $Fe_7(N_{0.75}C_{0.25})_3$	-82.46	91.0	218	5.15
hcp-type Fe	-8.186	10.2	290	4.56

Table S5 Lattice parameters of ε-type $Fe_4(N_{0.6}C_{0.4})$ in run-1 at high pressures and room T.

P (GPa)	V (Å^3)	a (Å)	c (Å)
1.0(1)	80.55(2)	4.6321(8)	4.3348(9)
2.2(1)	79.80(4)	4.622(1)	4.314(1)
3.1(1)	79.50(3)	4.617(1)	4.306(1)
4.4(1)	78.79(3)	4.603(1)	4.294(1)
5.8(1)	77.90(3)	4.5846(9)	4.280(1)
8.3(1)	76.53(4)	4.558(1)	4.253(1)
9.4(1)	76.05(4)	4.548(1)	4.245(1)
10.7(1)	75.59(4)	4.539(1)	4.236(1)
12.0(1)	74.98(5)	4.527(1)	4.225(1)
13.8(3)	74.20(5)	4.510(1)	4.212(1)
15.8(3)	73.41(8)	4.493(2)	4.198(2)
17.3(3)	72.88(8)	4.483(2)	4.187(2)
19.0(3)	72.33(6)	4.472(2)	4.177(1)
20.7(3)	71.87(7)	4.462(2)	4.168(1)
22.3(3)	71.36(8)	4.453(2)	4.156(2)
24.4(3)	70.63(6)	4.436(2)	4.144(1)
25.9(3)	70.23(4)	4.426(1)	4.138(1)
27.4(3)	69.95(5)	4.422(1)	4.131(1)
29.2(3)	69.59(6)	4.415(2)	4.123(2)

Table S6 Lattice parameters of ε-type Fe$_7$(N$_{0.75}$C$_{0.25}$)$_3$ in runs 2-4 at high P-T conditions.

P (GPa)	T (K)	V (Å^3)	a (Å)	c (Å)	P (GPa)	T (K)	V (Å^3)	a (Å)	c (Å)
run-2					run-3				
0.0001	300	85.01(1)	4.7309(1)	4.3857(2)	0.4(1)	300	84.70(3)	4.7250(5)	4.380(2)
0.5(1)	300	84.83(2)	4.7270(3)	4.383(1)	1.6(1)	300	84.09(8)	4.717(2)	4.365(5)
1.3(1)	300	84.57(3)	4.7210(5)	4.381(2)	2.8(1)	300	83.64(10)	4.710(2)	4.355(6)
2.2(1)	300	83.97(8)	4.712(1)	4.368(4)	4.8(1)	300	82.68(6)	4.688(1)	4.345(3)
3.4(1)	300	83.40(2)	4.7010(3)	4.358(1)	21.6(2)	450(5)	77.33(5)	4.574(1)	4.269(3)
4.3(1)	300	82.97(6)	4.692(1)	4.351(3)	24.1(2)	600(5)	76.92(5)	4.563(1)	4.266(3)
5.6(1)	300	82.30(4)	4.682(3)	4.335(2)	27.2(2)	750(5)	76.29(4)	4.551(1)	4.253(3)
7.2(1)	300	81.80(3)	4.6670(6)	4.337(2)	22.8(2)	300	76.55(4)	4.558(1)	4.254(2)
8.6(1)	300	81.26(5)	4.658(1)	4.325(3)	23.8(2)	300	76.34(2)	4.554(1)	4.251(2)
10.0(1)	300	80.82(3)	4.6480(5)	4.321(2)	25.8(2)	450(5)	75.98(5)	4.542(1)	4.252(3)
11.5(1)	300	80.22(2)	4.6380(5)	4.307(1)	28.2(2)	600(5)	75.64(3)	4.534(1)	4.249(2)
13.1(1)	300	79.65(4)	4.6250(8)	4.299(2)	30.1(2)	750(5)	75.44(3)	4.531(1)	4.243(2)
14.9(1)	300	79.06(7)	4.615(1)	4.286(4)	34.1(2)	450(5)	73.91(4)	4.497(1)	4.220(3)
16.2(1)	300	78.54(5)	4.604(1)	4.279(3)	35.9(2)	600(5)	73.77(4)	4.496(1)	4.214(3)
18.0(1)	300	78.00(8)	4.594(1)	4.267(5)	36.5(2)	750(5)	73.91(6)	4.502(1)	4.211(4)
19.6(1)	300	77.48(5)	4.582(1)	4.261(3)	33.7(2)	450(5)	73.95(5)	4.498(1)	4.222(4)
21.7(1)	300	76.94(5)	4.570(1)	4.255(3)	34.6(2)	600(5)	73.97(6)	4.500(1)	4.217(4)
23.1(1)	300	76.50(6)	4.561(1)	4.247(3)	35.5(2)	750(5)	74.06(6)	4.503(1)	4.217(4)
24.8(1)	300	76.00(5)	4.550(1)	4.239(3)	29.7(2)	300	74.62(7)	4.517(2)	4.224(5)
26.2(1)	300	75.61(5)	4.541(1)	4.234(3)	39.4(2)	300	72.49(7)	4.472(2)	4.185(5)
27.8(1)	300	75.20(7)	4.531(2)	4.230(4)	39.5(2)	450(5)	72.72(5)	4.473(1)	4.197(3)
29.4(1)	300	74.73(6)	4.522(1)	4.221(4)	42.0(2)	600(5)	72.44(8)	4.469(2)	4.188(5)
30.7(1)	300	74.36(8)	4.513(2)	4.217(5)	run-4				
33.3(1)	300	73.76(5)	4.499(1)	4.208(3)	27(2)	300	76.22(9)	4.561(3)	4.231(5)

Table S7 Summary of thermal equation of state parameters of ε-type Fe nitrides and carbonitrides (Adler and Williams, 2005; Litasov et al., 2014, 2017; Lv et al., 2020; Yin et al., 2014). The numbers in parenthesis are uncertainties.

ε-type phase	V_0 (Å^3)	K_0 (GPa)	K_0'	$\partial K/\partial T$ (GPa/K)	$\alpha_0 \times 10^{-5}$ (K^{-1})	$\alpha_1 \times 10^{-8}$ (K^{-2})	References
$Fe_4(N_{0.6}C_{0.4})$	81.11(7)	133(2)	4 (fixed)				This study
$Fe_7(N_{0.75}C_{0.25})_3$	85.00(1)	177(1)	4 (fixed)	-0.02(1)	3.3(8)	---	This study
Fe_7N_3	86.04(10)	168(10)	5.7(1.5)				Adler and Williams, 2005
Fe_7N_3	86.18(2)	163(2)	5.3(2)	-0.032(1)	3.60(12)	1.56(16)	Litasov et al., 2017
$Fe_3N_{0.8}$	81.44(2)	157(3)	5.3 (fixed)	-0.035(1)	3.74(13)	1.37(25)	Litasov et al., 2014
Fe_7N_3	86.55(2)	160(2)	4.3(2)				Lv et al., 2020
Fe_3N	85.38(1)	154(2)	4 (fixed)				Yin et al., 2014

Table S8 Lattice parameters of h-type $Fe_7(N_{0.75}C_{0.25})_3$ in runs 3-4 at high P-T conditions.

P (GPa)	T (K)	V (Å^3)	a (Å)	c (Å)
		run-3		
45.5(3)	750(5)	161.1(1)	6.592(2)	4.281(2)
40.5(3)	300	161.88(9)	6.602(1)	4.289(2)
42.1(3)	300	161.28(9)	6.594(2)	4.283(1)
43.0(3)	300	161.0(1)	6.589(2)	4.282(3)
44.1(3)	300	160.62(9)	6.584(1)	4.278(2)
45.2(3)	300	160.18(6)	6.578(1)	4.274(1)
44.8(3)	450(5)	160.65(7)	6.587(1)	4.276(1)
45.4(3)	600(5)	160.7(1)	6.585(2)	4.280(2)
46.4(3)	750(5)	160.7(1)	6.585(3)	4.280(3)
46.3(3)	300	159.74(6)	6.573(1)	4.269(1)
48.1(3)	300	159.05(5)	6.564(1)	4.262(1)
49.7(3)	300	158.5(1)	6.557(1)	4.256(2)
51.4(3)	300	158.0(1)	6.551(1)	4.251(2)
50.4(3)	450(5)	158.55(8)	6.557(1)	4.258(1)
51.2(3)	600(5)	158.6(1)	6.558(1)	4.259(2)
52.9(3)	750(5)	158.3(1)	6.556(2)	4.253(2)
52.2(3)	300	157.7(1)	6.547(2)	4.247(2)
53.4(3)	300	157.21(6)	6.541(1)	4.243(1)
54.5(3)	300	156.9(1)	6.538(1)	4.239(2)
55.7(3)	300	156.6(1)	6.534(2)	4.236(2)
52.7(3)	450(5)	157.8(1)	6.546(1)	4.251(2)
54.0(3)	600(5)	157.6(1)	6.546(1)	4.248(2)
55.0(3)	750(8)	157.5(1)	6.545(2)	4.244(2)
44.7(3)	300	160.1(1)	6.578(2)	4.272(2)
29.3(3)	300	166.7(2)	6.669(3)	4.329(3)
27.1(3)	300	167.9(1)	6.679(2)	4.345(2)
		run-4		
42(2)	300	161.7(2)	6.599(3)	4.289(3)
57(2)	300	157.1(2)	6.542(3)	4.239(3)

Table S9 Summary of equation of state parameters of h-type $Fe_7(N_{0.75}C_{0.25})_3$ and related compounds (Chen et al., 2012; Kusakabe et al., 2019; Liu et al., 2016a; Minobe et al., 2015; Nakajima et al., 2011).

Phase	V_0 (Å^3)	K_0 (GPa)	K_0'	References
$Fe_7(N_{0.75}C_{0.25})_3$	182.4(7)	268(9)	4 (fixed)	Only comp.*, this study
$Fe_7(N_{0.75}C_{0.25})_3$	180.9(6)	306(9)	3.2 (fixed)	Only comp., this study
Fe_7N_3	185.2(1.0)	246(9)	4 (fixed)	Minobe et al., 2015
Fe_7N_3	184.5(5)	256(6)	4 (fixed)	Kusakabe et al., 2019
Fe_7N_3	181.4(5)	316(5)	3.2 (fixed)	Kusakabe et al., 2019
Fe_7C_3	184.2(3)	253(7)	3.6(2)	PM phase**, Nakajima et al., 2011
Fe_7C_3	184.69(16)	201(12)	8.0(1.4)	PM phase, Chen et al., 2012
Fe_7C_3	182.87(38)	307(6)	3.2(1)	NM phase***, Chen et al., 2012
Fe_7C_3	184.6(5)	196(9)	4.9(2)	PM phase, Liu et al., 2016a

* "Only comp." means that the EoS of h-type $Fe_7(N_{0.75}C_{0.25})_3$ is calculated only using the P-V data during compression in run-3.

** PM represents the paramagnetic state.

*** NM represents the nonmagnetic state.

Supplementary references

Adler, J. F., & Williams, Q. (2005). A high-pressure X-ray diffraction study of iron nitrides: Implications for Earth's core. *Journal of Geophysical Research: Solid Earth*, *110*, B01203. https://doi.org/10.1029/2004JB003103

Chen, B., Gao, L., Lavina, B., Dera, P., Alp, E. E., Zhao, J., & Li, J. (2012). Magneto-elastic coupling in compressed Fe_7C_3 supports carbon in Earth's inner core. *Geophysical Research Letters*, *39*(18), L18301. https://doi.org/10.1029/2012GL052875

Kusakabe, M., Hirose, K., Sinmyo, R., Kuwayama, Y., Ohishi, Y., & Helffrich, G. (2019). Melting curve and equation of state of β-Fe_7N_3: Nitrogen in the core? *Journal of Geophysical Research: Solid Earth*, *124*(4), 3448-3457. https://doi.org/10.1029/2018JB015823

Litasov, K. D., Shatskiy, A. F., Ovchinnikov, S. G., Popov, Z. I., Ponomarev, D. S., & Ohtani, E. (2014). Phase transformations of iron nitrides Fe_3N-Fe_4N studied by in situ X-ray diffractions. *JETP Letters*, *98*(12), 805-808. https://doi.org/10.1134/S0021364013250140

Litasov, K. D., Shatskiy, A., Ponomarev, D. S., & Gavryushkin, P. N. (2017). Equations of state of iron nitrides ε-Fe_3N_x and γ-Fe_4N_y to 30 GPa and 1200 K and implication for nitrogen in the Earth's core. *Journal of Geophysical Research: Solid Earth*, *122*(5), 3574-3584. https://doi.org/10.1002/2017JB014059

Liu, J., Li, J., & Ikuta, D. (2016a). Elastic softening in Fe_7C_3 with implications for Earth's deep carbon reservoirs. *Journal of Geophysical Research: Solid Earth*, *121*(3), 1514-1524. https://doi.org/10.1002/2015JB012701

Lv, M., Liu, J., Zhu, F., Li, J., Zhang, D., Xiao, Y., & Dorfman, S. M. (2020). Spin transitions and compressibility of ε-Fe_7N_3 and γ'-Fe_4N: Implications for iron alloys in terrestrial planet cores. *Journal of Geophysical Research: Solid Earth*, *124*, e2020JB020660. https://doi.org/10.1029/2020JB020660

Minobe, S., Nakajima, Y., Hirose, K., & Ohishi, Y. (2015). Stability and compressibility of a new iron-nitride β-Fe_7N_3 to core pressures. *Geophysical Research Letters*, *42*(13), 5206-5211. https://doi.org/10.1002/2015GL064496

Nakajima, Y., Takahashi, E., Sata, N., Nishihara, Y., Hirose, K., Funakoshi, K. I., & Ohishi, Y. (2011). Thermoelastic property and high-pressure stability of Fe_7C_3: Implication for iron-carbide in the Earth's core. *American Mineralogist*, *96*(7), 1158-1165. https://doi.org/10.2138/am.2011.3703

Prescher, C., Dubrovinsky, L., McCammon, C., Glazyrin, K., Nakajima, Y., Kantor, A., Merlini, M., & Hanfland, M. (2012). Structurally hidden magnetic transitions in Fe_3C at high pressures. *Physical Review B*, *85*(14), 140402. https://doi.org/10.1103/PhysRevB.85.140402

Yin, W., Lei, L., Jiang, X., Liu, P., Liu, F., Li, Y., Peng, F., & He, D. (2014). High pressure synthesis and properties studies on spherical bulk ε-Fe₃N. *High Pressure Research*, *34*(3), 317-326. https://doi.org/10.1080/08957959.2014.944910